

*Sensitivity of the Brewer-Dobson  
circulation and polar vortex variability to  
parametrized nonorographic gravity-wave  
drag in a high-resolution atmospheric  
model*

Article

Accepted Version

Polichtchouk, I., Shepherd, T. G., Hogan, R. J. and Bechtold, P. (2018) Sensitivity of the Brewer-Dobson circulation and polar vortex variability to parametrized nonorographic gravity-wave drag in a high-resolution atmospheric model. *Journal of the Atmospheric Sciences*. ISSN 1520-0469 doi: <https://doi.org/10.1175/jas-d-17-0304.1> (In Press) Available at <http://centaur.reading.ac.uk/75485/>

It is advisable to refer to the publisher's version if you intend to cite from the work.

To link to this article DOI: <http://dx.doi.org/10.1175/jas-d-17-0304.1>

Publisher: American Meteorological Society

All outputs in CentAUR are protected by Intellectual Property Rights law, including copyright law. Copyright and IPR is retained by the creators or other

copyright holders. Terms and conditions for use of this material are defined in the [End User Agreement](#).

[www.reading.ac.uk/centaur](http://www.reading.ac.uk/centaur)

## **CentAUR**

Central Archive at the University of Reading

Reading's research outputs online

1 **Sensitivity of the Brewer-Dobson circulation and polar vortex variability to**  
2 **parametrized nonorographic gravity-wave drag in a high-resolution**  
3 **atmospheric model**

4 I. Polichtchouk\*

5 *Department of Meteorology, University of Reading, Reading, UK*

6 *European Centre for Medium-Range Weather Forecasts, Reading, UK*

7 T. G. Shepherd

8 *Department of Meteorology, University of Reading, Reading, UK*

9 R. J. Hogan

10 *European Centre for Medium-Range Weather Forecasts, Reading*

11 *Department of Meteorology, University of Reading, Reading, UK*

12 P. Bechtold

13 *European Centre for Medium-Range Weather Forecasts, Reading, UK*

14 \*Corresponding author address: I. Polichtchouk, Department of Meteorology, University of Read-  
15 ing, Earley Gate, PO Box 243, Reading, RG6 6BB, UK.

16 E-mail: i.polichtchouk@reading.ac.uk

## ABSTRACT

17 The role of parametrized nonorographic gravity wave drag (NOGWD) and  
18 its seasonal interaction with the resolved wave drag in the stratosphere has  
19 been extensively studied in low-resolution (coarser than  $1.9^\circ \times 2.5^\circ$ ) climate  
20 models but is comparatively unexplored in higher-resolution models. Using  
21 the European Centre for Medium-Range Weather Forecasts Integrated Fore-  
22 cast System at  $0.7^\circ \times 0.7^\circ$  resolution, the wave drivers of the Brewer-Dobson  
23 circulation are diagnosed and the circulation sensitivity to the NOGW launch  
24 flux is explored. NOGWs are found to account for nearly 20% of the lower-  
25 stratospheric Southern Hemisphere (SH) polar cap downwelling and for less  
26 than 10% of the lower-stratospheric tropical upwelling and Northern Hemi-  
27 sphere (NH) polar cap downwelling. Despite these relatively small numbers,  
28 there are complex interactions between NOGWD and resolved wave drag, in  
29 both polar regions. Seasonal cycle analysis reveals a temporal offset in the re-  
30 solved and parametrized wave interaction: The NOGWD response to altered  
31 source fluxes is largest in mid-winter, while the resolved wave response is  
32 largest in the late winter and spring. This temporal offset is especially promi-  
33 nent in the SH. The impact of NOGWD on sudden stratospheric warming  
34 (SSW) life-cycles and the final warming date in the SH is also investigated.  
35 An increase in NOGWD leads to an increase in SSW frequency, reduction in  
36 amplitude and persistence, and an earlier recovery of the stratopause follow-  
37 ing a SSW event. The SH final warming date is also brought forward when  
38 NOGWD is increased. Thus, NOGWD is still found to be a very important  
39 parameterization for stratospheric dynamics even in a high-resolution atmo-  
40 spheric model.

## 41 **1. Introduction**

42 The wave-driven stratospheric overturning circulation, with air rising and dynamically cooling  
43 in the tropics and descending and dynamically warming in the extratropics, exerts a crucial control  
44 on stratospheric temperature and thereby on winds (e.g., Shepherd (2000)). It also plays a key role  
45 in the transport of water vapor, ozone and other chemical species. This mass transport circulation  
46 is named the Brewer-Dobson circulation (BDC). Faithfully representing the BDC in numerical  
47 weather and climate prediction models is vital for accurate stratospheric temperature distribution  
48 and chemistry. Accurate representation of stratospheric circulation, in turn, is important for tro-  
49 pospheric predictability on medium-range and seasonal timescales (e.g., Baldwin and Dunkerton  
50 2001; Douville 2009; Sigmond et al. 2013), as well as for getting the correct background informa-  
51 tion into the data assimilation system, given the deep weighting functions of the operational nadir  
52 temperature sounders (e.g., Polavarapu et al. 2005).

53 Rossby and gravity wave breaking and saturation in the middle atmosphere drives the BDC  
54 (for a review on the BDC see e.g., Butchart (2014)). In most models, small scale orographic and  
55 nonorographic gravity wave breaking and saturation is parametrized (for a review on gravity waves  
56 and their parametrization in models see e.g., Fritts and Alexander (2003); Plougonven and Zhang  
57 (2014)). From now on the term “NOGWD” will refer to parametrized nonorographic gravity wave  
58 drag and “OGWD” to parametrized orographic gravity wave drag. OGWD is an important source  
59 of stratospheric drag in both hemispheres in low resolution models (e.g., McLandress and Shep-  
60 herd 2009a; McLandress et al. 2012), with NOGWD playing a lesser role. However, the role of  
61 parametrized wave drag should diminish at higher resolution when the wave drag is increasingly  
62 resolved by the model. Therefore, the first aim of this study is to diagnose the role of the pa-  
63 rameterized waves in driving the tropical upwelling and polar cap downwelling at relatively high

64 horizontal resolution using the European Centre for Medium-Range Weather Forecasts (ECMWF)  
65 Integrated Forecast System (IFS). The downward-control principle of Haynes et al. (1991), which  
66 expresses the BDC as a response to breaking and saturating waves aloft, is used to separate the  
67 drivers of the BDC into OGWD, NOGWD and resolved wave drag. Thus far, such a separation  
68 has only been carried out for low horizontal (coarser than  $1.9^\circ \times 2.5^\circ$ ) and vertical (coarser than  
69 1 km in the lower stratosphere) resolution stratosphere resolving climate models.

70 Diagnostically, OGWD is found to be a minor contributor to drag in the IFS at TL255L137  
71 resolution (80 km in the horizontal and  $\sim 300$  m in the vertical in the lower stratosphere) whereas  
72 NOGWD remains important, especially in the SH. Therefore, the second aim of this study is to  
73 assess the impact of NOGWD flux perturbations on the strength of the BDC, and on the resolved  
74 wave drag over the seasonal cycle. The seasonal cycle has received relatively little attention in the  
75 studies of parametrized and resolved wave drag interaction (e.g., Cohen et al. 2013, 2014; Sigmond  
76 and Shepherd 2014), which have focused on the time-mean response. In the SH stratosphere, the  
77 resolved and parametrized wave drag exhibit distinct seasonality: the resolved wave drag max-  
78 imizes in late winter/spring (Randel 1988; Quintanar and Mechoso 1995) and the parametrized  
79 wave drag in mid-winter (Pulido and Thuburn 2008). Shaw et al. (2009) studied the interaction  
80 between reduced parametrized GWD (via lowering the upper boundary condition) and resolved  
81 drag in the context of the seasonal cycle in polar regions in the Canadian Middle Atmosphere  
82 Model (CMAM) at low resolution. The study found that reducing parametrized GWD altered re-  
83 solved wave drag leading to polar cap upper-stratospheric downwelling changing to upwelling in  
84 the NH, and to a shift of maximum downwelling from November to December in the SH. The  
85 final aim of this study is to develop those concepts further with a high-resolution model and in the  
86 context of NOGWD perturbations. For example, the dominant NH drag in CMAM was OGWD,

87 and this will have a very different response to wind changes than NOGWD which has a broad  
88 phase speed spectrum.

89 Climatologically, NOGWD perturbations have a relatively small effect on the NH BDC in the  
90 IFS. However, NOGWD has a significant impact on the temporal evolution of polar dynamics,  
91 which is investigated here in the context of NH stratospheric sudden warming (SSW) life-cycles  
92 and in particular Arctic polar night jet oscillation (PJO) events, which are long lived and have  
93 a stronger influence on the troposphere than other SSWs (Hitchcock et al. 2013; Hitchcock and  
94 Shepherd 2013; Hitchcock and Simpson 2014).

95 The paper is organized as follows. Section 2 briefly reviews the model, the experimental setup  
96 and the diagnostics used. Section 3 reviews the middle atmosphere momentum budget in the  
97 control run. In section 4, the BDC—split into its different wave drivers—is diagnosed for the  
98 control run with the free-running model. The impact of NOGWD flux on the BDC climatology  
99 and seasonal cycle is also discussed in this section. In section 5, the impact of NOGWD on the  
100 SSWs in the NH is discussed. Finally, a summary and conclusions are given in section 6.

## 101 **2. Methods**

### 102 *a. Model description and setup*

103 The IFS is a global semi-Lagrangian pseudo-spectral model developed and used for operational  
104 forecasts. The detailed description of its dynamical core and the physical parameterizations — as  
105 used in cycle CY43R1— can be found in ECMWF (2016). Here, IFS is run at TL255 spectral  
106 truncation with a linear Gaussian grid (grid spacing of  $\sim 80$  km) and a time-step size of 1800 s.  
107 The vertical domain is discretized into 137 levels (the resolution is  $\sim 300$  m at 100 hPa, coarsening  
108 to  $\sim 1.5$  km at 1 hPa) and the model top is located at 0.01 hPa. To prevent wave reflection at the



109 model top, a fourth order hyper-diffusion ( $\nabla^4$ ) is applied on vorticity, divergence and temperature  
110 fields above 10 hPa to damp vertically propagating waves. The hyper-diffusion  $e$ -folding timescale  
111 on the largest resolved wavenumber decreases from 0.65h at 10 hPa to 0.03h at the model top. In  
112 addition, a first order diffusion ( $\nabla$ ) is applied on the divergence field only above 1 hPa. The  
113 diffusion  $e$ -folding timescale on the largest resolved wavenumber decreases from 0.1h at 1 hPa to  
114 0.02h at the model top. Both “sponges” damp the zonal-mean fields (i.e., apply diffusion on the  
115 zonal wavenumber  $m = 0$  coefficients).

116 The nonorographic gravity wave drag parameterization in the IFS follows Scinocca (2003). Orr  
117 et al. (2010) discuss in detail the specific implementation and beneficial effect of this parametriza-  
118 tion on the middle atmosphere circulation in the IFS. In the default setting, the momentum source  
119 is represented by a broad spectrum of wave speeds (half-width of  $150 \text{ ms}^{-1}$ ) discretized into 25  
120 variable-resolution phase-speed bins and launched at 450 hPa. The 450 hPa launch level implies  
121 that NOGWs can break in the upper-troposphere and lower-stratosphere on encountering criti-  
122 cal levels, such as when the subtropical jets terminate in the lower stratosphere. The orographic  
123 gravity wave drag parameterization in the IFS follows Lott and Miller (1997).

124 Two different experimental protocols are followed: (1) an ensemble of four-year forecasts; and  
125 (2) nudged seven-month forecasts, where the troposphere below 500 hPa is nudged towards ERA-  
126 Interim reanalyses (Dee et al. 2011) to constrain planetary and synoptic wave forcing from the  
127 troposphere. The “free-running” setup (1) allows us to answer the question of how the model  
128 statistics respond to NOGWD changes. Setup (2) allows us to study the response of internal  
129 middle atmosphere dynamics to changes in NOGWD, specifically to reproduce the evolution of  
130 the 2006 PJO life-cycle. All simulations are forced by prescribed daily-varying observed sea-  
131 surface temperatures.

132 In the free-running setup, eight four-year forecasts are initialized one year apart with the first  
133 forecast starting on 1 August 2004. The first month is disregarded as a spin-up period. This  
134 procedure samples years from 2004 to 2015 and generates 32 (non-independent) years of data.  
135 Three simulations are performed, one with the default NOGWD launch spectrum amplitude of  
136 3.75 mPa, one with the NOGWD launch spectrum amplitude reduced to 1 mPa, and one with the  
137 NOGWD launch spectrum amplitude increased to 14 mPa. The study of such a broad range of  
138 flux amplitudes is motivated by Scheffler and Pulido (2017) who find, using a data-assimilation  
139 technique, that the optimal launch momentum flux in the SH lower-stratosphere can fluctuate  
140 between four to 0.25 times the reference value over the seasonal cycle. In all cases the amplitude  
141 of the launch spectrum is reduced in amplitude by 75% in the tropics<sup>1</sup>.

142 In the nudged setup, relative vorticity and temperature fields are relaxed via Newtonian relax-  
143 ation to the ERA-Interim reanalysis fields on the terrain-following model levels below 500 hPa.  
144 The fields only up to total wavenumber 61 in the spherical harmonic expansion are nudged. The  
145 relaxation timescale is 12 h for relative vorticity and 5 days for temperature. To study the 2006  
146 PJO life-cycle, forecasts with five ensemble members each are started on 1 November 2005. As  
147 in the free-running setup, three forecasts with different NOGWD launch spectrum amplitudes are  
148 performed.

149 Henceforth, all forecasts using the default NOGWD launch amplitude will be referred to as the  
150 “control run”, the reduced NOGWD launch amplitude as the “reduced NOGWD run”, and the  
151 increased NOGWD launch amplitude as the “increased NOGWD run”.

152 Fields are output every 6h to sample the diurnal cycle. As noted in Seviour et al. (2012) and  
153 Sakazaki et al. (2015) there is a strong diurnal cycle in the zonal-mean fields in the stratosphere –

---

<sup>1</sup>It should be noted that in the operational IFS cycle 43R1 the launch spectrum is reduced in amplitude by 25% in the tropics.

154 especially in the tropics – that is associated with thermal tides. This is observed in all model runs  
 155 with the IFS.

## 156 *b. Diagnostics*

### 157 1) RESIDUAL MEAN MERIDIONAL CIRCULATION

158 The Transformed Eulerian Mean framework is used to diagnose the residual mean meridional  
 159 circulation (Andrews et al. 1987). The residual mean mass streamfunction  $\Psi$  is:

$$\Psi \equiv -\frac{\cos \phi}{g} \int_p^0 \bar{v}^*(\phi, p') dp', \quad (1)$$

160 where the residual meridional velocity  $\bar{v}^*$  is

$$\bar{v}^* = \bar{v} - \frac{\partial}{\partial p} \left( \frac{\overline{v'\theta'}}{\partial \theta / \partial p} \right) \quad (2)$$

161 with  $\overline{(\cdot)}$  denoting the zonal-mean and  $(\cdot)'$  the deviation of a field from the zonal-mean,  $v$  is merid-  
 162 ional velocity,  $\theta$  is potential temperature,  $p$  is pressure,  $\phi$  latitude,  $g$  gravitational acceleration,  
 163 and at  $p = 0$ ,  $\Psi = 0$  is imposed.

164 To diagnose the contributions of OGWD and NOGWD (recall these refer to the parametrized  
 165 waves) and the resolved wave drag in driving the residual mean meridional circulation, the  
 166 downward-control principle of Haynes et al. (1991) is used. It expresses the steady residual mean  
 167 meridional circulation as a response to drag from breaking/saturating waves aloft.

168 The downward-control streamfunction  $\Psi_{\text{DC}}$  is:

$$\Psi_{\text{DC}} \equiv \frac{\cos \phi}{g} \int_p^0 \frac{\bar{D}(\phi, p')}{f - (a \cos \phi)^{-1} \partial(\bar{u} \cos \phi) / \partial \phi} dp', \quad (3)$$

169 where  $a$  is the Earth's radius,  $f$  is the Coriolis parameter,  $u$  is zonal wind, and  $\bar{D}$  is the zonal-mean  
 170 wave drag composed of the tendency terms in the zonal momentum equation due to the resolved  
 171 wave drag and NOGWD and OGWD. Resolved wave drag is given by  $\nabla \cdot \mathbf{F} / a \cos \phi$ , where  $\mathbf{F}$  is

172 the Eliassen-Palm (EP) flux

$$\mathbf{F} = \{F_\phi, F_p\} = a \cos \phi \left( \frac{\overline{\theta'v'} \partial \bar{u} / \partial p}{\partial \bar{\theta} / \partial p} - \overline{u'v'}, \frac{\overline{\theta'v'}}{\partial \bar{\theta} / \partial p} \left( f - \frac{1}{a \cos \phi} \frac{\partial \bar{u} \cos \phi}{\partial \phi} \right) - \overline{u'\omega'} \right), \quad (4)$$

173 where  $\omega$  is vertical ‘‘pressure’’ velocity. Note that  $\nabla \cdot \mathbf{F} / a \cos \phi$  includes orographic and nonoro-  
 174 graphic gravity wave drag by waves directly resolved by the dynamical core. The effective hori-  
 175 zontal resolution, inferred from the kinetic energy spectrum in the lower stratosphere, is up to total  
 176 wavenumber  $\sim 80$ .

177 The residual vertical velocity  $\bar{w}^*$  is computed following McLandress and Shepherd (2009a):

$$\bar{w}^* = \frac{gH}{pa \cos \phi} \frac{\partial \Psi}{\partial \phi}, \quad (5)$$

178 where  $H$  is the pressure scale height  $H = 7$  km. Similarly,  $\bar{w}_{\text{DC}}^*$  can be calculated from  $\Psi_{\text{DC}}$ .

179 The vertical mass flux across a pressure surface poleward of latitude  $\phi$  in the NH and SH is  
 180 given by Holton (1990):

$$F_{\text{NH}} = 2\pi a^2 \rho \int_{\phi}^{\pi/2} \bar{w}_{\text{DC}}^* \cos \phi d\phi \quad (6)$$

181 and

$$F_{\text{SH}} = 2\pi a^2 \rho \int_{-\pi/2}^{\phi} \bar{w}_{\text{DC}}^* \cos \phi d\phi, \quad (7)$$

182 where  $\rho$  is density. Instead of evaluating the integral in (3) on constant angular momentum con-  
 183 tours, it is evaluated at a constant latitude. This is a good approximation outside the tropics.  
 184 Expressed in terms of  $\Psi_{\text{DC}}$  and noting that  $\Psi_{\text{DC}}$  vanishes at the poles, the downward mass flux  
 185 poleward of latitude  $\phi$  is given by  $F_{\text{NH}} = 2\pi a \Psi_{\text{DC}}(\phi)$  and  $F_{\text{SH}} = -2\pi a \Psi_{\text{DC}}(\phi)$ . The upward  
 186 tropical mass flux between two latitudes  $\phi$  and  $-\phi$  is given by  $F_{\text{TR}} = 2\pi a \{\Psi_{\text{DC}}(\phi) - \Psi_{\text{DC}}(-\phi)\}$ .  
 187  $F_{\text{TR}}$  is calculated between the ‘turnaround’ latitudes as in McLandress and Shepherd (2009a) and  
 188 Butchart et al. (2011). The turnaround latitudes are located between the minimum and maximum  
 189 values of  $\Psi_{\text{DC}}$  (i.e., where the tropical upwelling changes to extratropical downwelling).

## 190 2) STRATOSPHERIC SUDDEN WARMINGS

191 For the free-running setup, composites of SSWs are constructed. Diagnostics similar to those  
192 described in McLandress and Shepherd (2009b) are used to identify SSWs. In particular, a SSW  
193 is said to occur when the daily mean zonal-mean zonal wind at 10 hPa and 60°N becomes easterly  
194 between November to March. The date at which this occurs is referred to as the central date. Final  
195 vortex breakdowns are excluded by requiring that following the SSW, the zonal wind must become  
196 westerly for at least 10 days before the end of April. To avoid counting the same SSW twice, the  
197 central dates must be separated by at least 60 days.

## 198 3) FINAL WARMING IN THE SH

199 The Black and McDaniel (2007) method is used to diagnose the final warming date in the SH. In  
200 particular, a final warming occurs when the zonal-mean zonal wind at 60°S falls below 10 m s<sup>-1</sup>  
201 and does not return to values above 10 m s<sup>-1</sup> before the next winter.

### 202 *c. Evaluation data sets*

203 To evaluate the nudged runs during the 2006 PJO event, version 3.3 of the temperature product  
204 from the Microwave Limb Sounder (MLS) instrument (Livesey et al. 2011) on-board the *Aura*  
205 satellite is used between December 2005 to May 2006. MLS has provided continuous observations  
206 of the middle atmosphere from September 2004 to the present day. The useful pressure range for  
207 the temperature observations is 261–0.001hPa. The vertical resolution of MLS data is 5 km. In  
208 addition, gradient wind balance zonal winds derived from MLS temperature data are used for  
209 evaluation.

210 The SSW and the SH final warming date statistics in the free-running model are evaluated  
211 against the ERA-Interim reanalysis statistics.

### 212 3. Zonal momentum budget in the control run

213 Before diagnosing the BDC, it is useful to document the distribution of parametrized and re-  
214 solved wave drag in the middle atmosphere for this version of the IFS. The momentum budget  
215 for the IFS at TL159L91 resolution has been diagnosed and discussed for July and December by  
216 Orr et al. (2010). The momentum budget at TL255L137 resolution is shown in Fig. 1 for different  
217 seasons for the control run. The key features are:

- 218 • The zonal wind tendency due to resolved planetary waves (in shading, first column) and  
219 stationary parametrized OGWs (in shading, third column) reflects the fact that these waves  
220 can only propagate and break/saturate in the middle atmosphere when the background zonal  
221 winds are westerly. Zonal wavenumber decomposition shows that most of the resolved wave  
222 drag is coming from wavenumbers one to three (not shown). This is true even in the meso-  
223 sphere as the strong sponge applied above 1 hPa is very effective in damping the higher-  
224 frequency smaller-scale resolved waves. The resolved wave drag is stronger in the NH. It is  
225 maximal in the NH in mid-winter, but in the SH in late winter/spring. This temporal asym-  
226 metry is consistent with observations (e.g., Randel 1988; Quintanar and Mechoso 1995) and  
227 the theory of Charney and Drazin (1961), which states that planetary waves can propagate  
228 into the middle atmosphere when the background westerlies are less than a threshold value.  
229 This value is generally below the SH mid-winter westerly wind speed.
- 230 • In the tropical lower stratosphere, the resolved wave drag consists mostly of synoptic and  
231 transient planetary wave breaking on the equatorward flank of the subtropical jet. These  
232 waves break throughout the year and are important in driving the tropical upwelling (Randel  
233 et al. 2008).

- 234 • NOGWs (in shading, second column) are filtered by the background zonal wind: The west-  
235 ward propagating waves are filtered by the easterlies and the eastward propagating waves by  
236 the westerlies (e.g., Shepherd 2000) leading to eastward drag and polar ascent in the summer  
237 mesosphere and westward drag and polar descent in the winter mesosphere. In the sum-  
238 mer hemisphere, NOGWD dominates the mesospheric drag as the resolved gravity waves are  
239 removed by the strong sponge before they reach the mesosphere.
- 240 • NOGWD is largest in the SH, where it is the dominant parametrized wave forcing, because  
241 of stronger preferential filtering of eastward vs westward propagating waves. In contrast to  
242 what is found in lower-resolution models, OGWD is only stronger than NOGWD during the  
243 NH winter in the lower mesosphere. The integrand in (3) is density weighted, so the waves  
244 exerting drag at altitudes further above the stratosphere have less impact on the BDC. Given  
245 the above, the effect of the NOGWD flux changes on the BDC, and in particular on the  
246 downwelling over the pole, is expected to be smaller in the NH winter than in the SH winter.

#### 247 **4. Results: Residual mean meridional circulation**

##### 248 *a. The control run: Time-mean circulation*

249 Figure 2 shows the annual-mean tropical upward mass flux (a) and the extended winter mean  
250 (October-May for the NH and March-November for the SH) downward mass flux over (b) the  
251 NH and (c) the SH polar caps for the control run. The extended winter period comprises all the  
252 months for which polar cap downwelling occurs. Both the total downward-control mass flux and  
253 the parametrized wave contribution are shown. The downward-control streamfunction and the  
254 direct streamfunction (i.e., eqn. 1) disagree slightly over the extended SH winter pole due to the  
255 transience of the vortex breakdown process (not shown).

256 Table 1 summarizes the resolved and parametrized wave partitioning in driving the tropical  
257 upwelling and extended winter polar cap downwelling in both hemispheres. At 70 hPa, parame-  
258 terized waves account for 7% of the total upwelling (5% OGWD and 2% NOGWD) decreasing  
259 to 0% (2.4% OGWD and -2.4% NOGWD) at 10 hPa. These figures should be compared to the  
260 multi-model inter-comparison of Butchart et al. (2011) where, on average, parameterized waves  
261 account for 28% of the upwelling (21.1% OGWD and 7.1% NOGWD) at 70 hPa and 25.6% (4.7%  
262 OGWD and 10.9% NOGWD) at 10 hPa. Given the higher horizontal resolution of the IFS com-  
263 pared to the models of Butchart et al. (2011) it is not surprising that the role of parameterized  
264 wave drag is smaller in the IFS than in these studies. Note that the relative role of parametrized  
265 waves in driving the upwelling increases as one approaches the troposphere in Fig. 2a. This is a  
266 result of the NOGWs being launched at 450 hPa and the westward propagating NOGWs breaking  
267 at the critical levels in the subtropics, where the subtropical jets terminate. Hence, the location of  
268 the NOGW launch level is likely to impact the parametrized waves that contribute to the tropical  
269 upwelling.

270 There are large differences in the parameterized wave downwelling magnitudes between the  
271 hemispheres. At 70 hPa, parameterized waves account for only 7% (all OGWD) of the total  
272 extended NH winter pole downwelling, while in the SH the similar figure is 19%. In the SH all  
273 of the parameterized downwelling is coming from NOGWD. This is expected from Fig. 1, which  
274 shows a much larger influence of NOGWD in the SH than in the NH. Generally, the ratio of the  
275 parameterized to resolved wave drag in driving the upwelling/downwelling decreases slightly with  
276 altitude in the tropics, and increases with altitude over the poles (see Table 1). The parameterized  
277 wave downwelling starts to dominate the resolved wave downwelling above 5 hPa in the SH and  
278 above 1 hPa in the NH.



279 *b. Sensitivity to nonorographic gravity wave drag: Time-mean circulation*

280 Given the importance of NOGWD at higher resolution, the sensitivity of tropical upwelling and  
281 polar cap downwelling to changes in NOGWD flux is now examined. Table 1 summarizes the  
282 changes to resolved and parametrized wave partitioning brought about by a decrease in NOGWD  
283 flux by 3.75 times and an increase in NOGWD flux by 3.75 times. As expected, the parametrized  
284 wave driving decreases (increases) with a decrease (increase) in NOGWD flux. For example, at  
285 70 hPa, the parametrized wave contribution to the tropical upwelling and NH polar cap down-  
286 welling reduces to 2% with a reduction in NOGWD flux. Similarly, the parametrized wave con-  
287 tribution to the 70 hPa tropical upwelling and NH polar cap downwelling increases to nearly 20%  
288 with an increase in NOGWD flux. For the SH polar cap downwelling, the corresponding figure is  
289 6% for a decrease in NOGWD flux and 45% for an increase in NOGWD flux.

290 Figure 2 shows the difference in (d) the annual-mean tropical upward mass flux and (e) the  
291 extended NH and (f) SH winter downward mass flux between the increased and reduced NOGWD  
292 runs. As expected from the dominance of NOGWD in the SH, varying NOGWD flux has the most  
293 impact there. In particular, the total downwelling (blue for the downward-control streamfunction)  
294 increases in response to increase in NOGWD (see Table 1). For example, increasing NOGWD flux  
295 from the control value by 3.75 times leads to a  $\sim 30\%$  increase in the SH polar cap downwelling at  
296 70 hPa. The net effect of the increased downwelling is to warm the SH stratospheric winter pole  
297 by  $\sim 15$  K (not shown). However, the response in the total downwelling is not directly proportional  
298 to the change in NOGWD induced downwelling (black lines) as the resolved wave downwelling  
299 (red lines) opposes the NOGWD changes in the time-mean. Interestingly, in the NH polar mid-  
300 and upper stratosphere and in the tropics, the decrease in the resolved wave driving in response to  
301 increase in NOGWD leads to a decrease in total downwelling (see Table 1).

302 To understand the changes in the resolved wave forcing, Figs. 3a-b show the difference in the  
303 extended NH and SH winter stratospheric EP flux and its divergence between the increased and  
304 reduced NOGWD runs. The resolved wave drag corresponds to EP flux convergence, hence the  
305 red regions indicate less resolved wave drag when NOGWD is increased. Over the polar vortex,  
306 the resolved wave response falls into two distinct regions: an increase in the resolved wave drag in  
307 the lower stratosphere and a decrease in the resolved wave drag in the mid- to upper stratosphere.  
308 This is reflected in the vertical profile of the response of the downwelling driven by the resolved  
309 waves in Fig. 2e and 2f (red lines).

310 To quantify the response in the resolved waves in the lower and upper stratosphere, an EP-flux  
311 budget (following Kushner and Polvani (2004)) is constructed for two boxes in the vicinity of  
312 the polar vortex between 35°N/S and 90°N/S: 1) a lower-stratospheric box from 70 to 10 hPa  
313 and 2) an upper-stratospheric/lower-mesospheric box from 10 to 0.1 hPa. The budget is shown  
314 for the increased (in red) and reduced (in green) NOGWD runs in Fig. 3c-d. In the winter lower  
315 stratosphere there is 5% more wave drag in the NH and 25% more wave drag in the SH in response  
316 to increased NOGWD. This likely occurs as a result of a weakened vortex — brought about by the  
317 increase in NOGWD — that is more amenable to wave breaking lower down. There is a marked  
318 reduction in the resolved waves entering (20% less in the NH and 25% less in the SH) and breaking  
319 (63% less wave breaking in the NH and 90% less wave breaking in the SH) in the mid- to upper  
320 stratosphere.

321 In summary, increasing NOGWD weakens the polar night jet and thereby decreases resolved  
322 wave propagation into the polar mid- to upper stratosphere during the extended winter season,  
323 leading to less resolved wave breaking there. This counteracts the polar cap downwelling increase  
324 by the NOGWD such that the total mid- to upper-stratospheric downwelling decreases in the NH  
325 and increases in the SH in response to increase in NOGWD. In the lower stratosphere the polar

326 cap downwelling increases in both hemispheres as the resolved waves reinforce the NOGWD  
327 perturbation.

328 *c. The control run: The seasonal cycle*

329 To understand how the partitioning of parameterized and resolved waves in driving the polar  
330 cap downwelling differs between seasons and between the hemispheres, it is useful to examine  
331 the seasonal cycle of the polar cap average  $\bar{w}_{DC}^*$ . Figure 4 shows the seasonal cycle of polar  
332 cap average  $\bar{w}_{DC}^*$  (thick solid lines, top panels) and its parameterized wave (dashed lines, bottom  
333 panels) and resolved wave (thin solid lines, bottom panels) contribution for the control simulation  
334 (black lines).

335 The upwelling in the summer mesosphere is mostly driven by NOGWD over both poles with  
336 little contribution from the resolved waves (not shown explicitly, but compare first and second  
337 columns of Fig. 1). In the NH, the downwelling is maximum in mid-winter in January and is pre-  
338 dominantly driven by resolved waves in the stratosphere (apart from the upper stratosphere where  
339 the parameterized waves dominate the downwelling in autumn). In the NH the parametrized wave  
340 downwelling is maximum during the stratospheric zonal wind maximum in the late autumn/early  
341 winter, whereas the maximum in the resolved wave downwelling is offset slightly in time. In con-  
342 trast, in the SH the downwelling is maximal in the spring season and the time of maximum down-  
343 welling occurs later as one descends through the stratosphere. The resolved waves dominate the  
344 downwelling in the spring season, whereas the parameterized waves dominate the downwelling in  
345 mid-winter in the mid- to upper stratosphere (see also Fig. 1), at the time of maximum westerlies.  
346 This seasonal behaviour of the resolved and parametrized waves is consistent with observations  
347 (e.g., Randel 1988; Quintanar and Mechoso 1995; Pulido and Thuburn 2008) and also observed in  
348 CMAM (Shaw et al. 2009). The different timing in the resolved and parameterized wave down-

349 welling will be important for the response in the seasonality of  $\overline{w}_{DC}^*$  to changes in NOGWD. Note  
350 that unlike in the lower-resolution models, OGWD does not contribute to the polar cap averaged  
351  $\overline{w}_{DC}^*$  in the SH (not shown).

352 *d. Sensitivity to nonorographic gravity wave drag: The seasonal cycle*

353 The time-mean response might paint a misleading picture of the interaction between the resolved  
354 and the parameterized waves as there is a strong seasonality in the BDC forcing. The seasonal  
355 cycle of the polar cap average  $\overline{w}_{DC}^*$ , together with its resolved and parameterized wave driving  
356 contributions, is also shown in Fig. 4 for the reduced NOGWD run (in red) and increased NOGWD  
357 (in blue). Figure 5 shows the seasonal cycle of the difference in the polar cap average  $\overline{w}_{DC}^*$  between  
358 the increased NOGWD and reduced NOGWD runs.

359 In the summer, the total  $\overline{w}_{DC}^*$  response in the upper stratosphere is proportional to changes in  
360 NOGWD as the easterlies filter out stationary planetary waves and smaller scale orographic gravity  
361 waves, leaving no resolved waves to interact with (see Fig. 1). Note that the seasonal transition  
362 from downwelling to upwelling occurs earlier in the increased NOGWD run, especially in the SH.  
363 This appears to be tied in with the onset of the final warming which occurs earlier in the increased  
364 NOGWD run; because the westerlies weaken earlier in the increased NOGWD run, the eastward  
365 propagating NOGWs can propagate into the upper stratosphere and mesosphere earlier. When the  
366 eastward propagating waves saturate they induce upwelling (see Fig. 4b).

367 To examine the effect of NOGWD on the final warming date, Fig. 6 shows the average of the  
368 final warming dates in the SH as a function of pressure together with the ERA-Interim climatology  
369 from 2004 to 2015 for reference (thick black dash-dotted line). As the NOGWD is increased, the  
370 climatological final warming date occurs earlier in the stratosphere as the vortex is weakened and  
371 is thus more amenable to wave breaking. This is consistent with more resolved wave drag in the

372 lower-stratosphere (see Fig. 3b). In the mesosphere, however, the vortex breakdown is delayed  
373 when the NOGWD is substantially increased. This is, as discussed above, due to the reduced re-  
374 solved wave drag entering the upper stratosphere and mesosphere. Resolved wave drag accelerates  
375 the seasonal evolution towards easterlies in the spring, so when it is reduced, the seasonal cycle  
376 is delayed. Note that the NOGWD tends to drag the zonal winds to zero at mid- to high-latitudes  
377 near the model top as the waves, originating at 450 hPa, are filtered such that only those with phase  
378 speeds of opposite sign to the zonal wind are left. Therefore NOGWD does not contribute to the  
379 vortex breakdown in the same way as the resolved waves. It should be emphasized that here the  
380 NOGWD is reduced via the sources, but the total resolved wave drag is largely unchanged, only  
381 its location is altered.

382 In the NH, OGWD partly compensates for the increase in NOGWD induced downwelling in  
383 winter (cf. dashed red, solid green and dash-dotted blue curves in Figs. 5a and 5c). The resolved  
384 wave drag shifts vertically in response to increase in the NOGWD induced downwelling in the  
385 mid- to upper stratosphere (cf. dotted lines in Figs. 5a and 5c), but there is a seasonal offset in  
386 the resolved wave response. As a result, the increase in net downwelling expected from increased  
387 NOGWD transitions to a decrease in downwelling towards the end of the extended winter season,  
388 in both the lower and middle stratosphere, and in both hemispheres.

389 The seasonal offset in the resolved wave response is larger in the SH, where the changes to  
390 NOGWD flux significantly modify the seasonal evolution of polar cap averaged  $\overline{w}_{DC}^*$ . When  
391 NOGWD is increased, it has the most impact in mid-winter in the SH when the resolved wave  
392 driving is weak in the stratosphere. Hence, the change in the SH total polar cap averaged  $\overline{w}_{DC}^*$  is  
393 almost proportional to NOGWD flux changes in mid-winter. Increasing NOGWD weakens and  
394 shifts the polar night jet equatorward. This leads to less resolved waves entering the mid- to up-  
395 per stratosphere—especially in the SH spring—resulting in less resolved wave downwelling (see

396 Fig. 5). The resolved waves appear to be unable to propagate as high into the stratosphere in the  
397 increased NOGWD run. As the parameterized wave downwelling is weak in the spring, the de-  
398 crease in the resolved wave downwelling dominates and results in a decrease in downwelling with  
399 increase in NOGWD. In the lower stratosphere (Figs. 5c-d), the resolved waves tend to amplify  
400 the NOGWD changes in mid-winter in both hemispheres, consistent with the increased wave drag  
401 in the mid-latitude lower stratosphere shown in Figs. 3 and 4.

## 402 **5. Results: SSWs**

403 Having examined the sensitivity of the BDC climatology to the NOGWD flux perturbations in  
404 the previous section, the next step is to assess the impact of these perturbations on SSWs, which  
405 are important for tropospheric predictability. In what follows the impact of NOGWD changes  
406 on the 2006 PJO life-cycle is first examined in the nudged setup before discussing the impact of  
407 NOGWD on SSWs in general.

### 408 *a. 2006 PJO event in the nudged model*

409 Figures 7a and 7b show the evolution of the gradient zonal-mean zonal wind averaged from  
410 50°N to 70°N and the polar-cap averaged zonal-mean temperature from MLS. In Figs. 7c and 7d  
411 the evolution of 50°N to 70°N ensemble-mean zonal-mean zonal wind and the polar cap averaged  
412 zonal-mean temperature is shown for the nudged control run. The nudged control run captures the  
413 2006 PJO life-cycle reasonably accurately, albeit the SSW occurs in the model two weeks earlier  
414 than in the observations (recall that the nudging is applied only below 500 hPa and the stratosphere  
415 evolves freely). That this is not an artifact of the ensemble averaging is shown in Fig. 7i, where the  
416 timeseries of the zonal-mean zonal wind at 60°N and 10 hPa is shown for all ensemble members  
417 of the control run. It is clear that all the ensemble members predict an earlier onset of the PJO

418 event than what is observed (MLS observations are shown in thick red line). The onset of the SSW  
419 is improved if the nudging is carried out below 100 hPa. The persistence length (quantified here  
420 by the number of days the zonal-mean zonal wind is easterly at 60°N and 10 hPa following the  
421 central date) of 24 days, however, is the same in the control run and in MLS.

422 The evolution of a typical long-lived SSW life-cycle has been described in detail (e.g., Siskind  
423 et al. 2010; Limpasuvan et al. 2012; Tomikawa et al. 2012; Hitchcock and Shepherd 2013; McLan-  
424 dress et al. 2013) and is summarized here for completeness. To aid the description of the life-cycle,  
425 the ensemble-mean zonal wind tendencies and the residual vertical velocity are shown in Fig. 8  
426 for the nudged control run (in shading, left column). The initial stratospheric warming is a result  
427 of enhanced resolved planetary wave drag (see Fig. 8e). As the zonal wind in the stratosphere  
428 becomes easterly during the PJO event, the westward propagating NOGWs, the resolved plane-  
429 tary waves and the OGWs are no longer able to enter the middle atmosphere. This, together with  
430 the transient response that generates an upward closing cell near the upper boundary, results in  
431 a weaker residual circulation and the concomitant cooling in the mesosphere (see also Fig. 4 in  
432 Ren et al. 2008). The middle atmosphere easterlies permit eastward phase-speed NOGWs to prop-  
433 agate upward resulting in the net eastward NOGWD. This contributes to the reformation of the  
434 polar night jet as the net eastward NOGWD induces upwelling and cooling of the polar regions.  
435 Following a PJO event, initially temperature evolves almost entirely diabatically as the resolved  
436 and the parametrized stationary orographic gravity wave forcing is suppressed. The descent of  
437 mesospheric cooling follows the vertical gradient in the climatological cooling profile and the  
438 radiative damping time, which decreases with decreasing pressure (see figure 2a and figure 10  
439 of Hitchcock and Shepherd 2013). As the westerlies in the mesosphere recover, the westward  
440 propagating NOGWs are no longer filtered out. On reaching the mesosphere, westward NOGWs  
441 induce downwelling and are hence responsible for the reformation of the stratopause which de-

442 scends downward with time. The short radiative damping time scales in the mesosphere imply  
443 that any temperature anomaly has to be maintained by dynamical heating. Once the stratospheric  
444 winds have become westerly throughout the stratosphere, OGWs can propagate into the middle  
445 atmosphere and contribute to the reformation of the stratopause by inducing dynamical heating.  
446 The persistence of the lower stratospheric warm anomaly following the PJO event is a result of  
447 strongly suppressed wave driving and weak climatological radiative cooling (see Figs. 12 and 10  
448 of Hitchcock and Shepherd 2013). This also removes any mechanism for chaotic error growth  
449 between troposphere and stratosphere.

450 Now the effect of changing NOGWD on the PJO life-cycle is examined. Figures 7e-h show  
451 the evolution of the 50°N to 70°N zonal-mean zonal wind and polar cap temperature for the re-  
452 duced NOGWD run and the increased NOGWD run. It is clear from the figure that the increased  
453 NOGWD run is unable to recreate the PJO event and instead produces two shallow and short-  
454 lived SSWs whose evolution is markedly different from the observations. The inability to recreate  
455 the PJO event in the increased NOGWD run results from the insufficient resolved wave forcing  
456 entering the stratosphere and markedly different basic state in the middle atmosphere.

457 Comparison of Fig. 7c to Fig. 7e and Fig. 7d to Fig. 7f reveals that reduction in NOGWD  
458 prolongs the persistence of the PJO event (from 24 days to 38 days, quantified by the number  
459 of days the zonal-mean zonal wind is easterly at 60°N and 10 hPa following the central date)  
460 and delays the reformation of the stratopause following the PJO event. This is made clearer by  
461 examining the difference in the zonal-mean zonal wind and the polar cap temperature between  
462 the reduced NOGWD run and the control run in Fig. 9a-b. To better understand the response  
463 of the PJO life-cycle to reduced NOGWD, the difference in the zonal wind tendencies and the  
464 residual vertical velocity between the reduced NOGWD run and the control run are shown in the  
465 left column of Fig. 8 (black and red contours).



466 Following the SSW, mesospheric westward NOGWD and the associated descent and adiabatic  
467 warming are suppressed in the reduced NOGWD run (Figs. 8a and 8g). Therefore temperature  
468 evolves more diabatically in the mesosphere and the cooling is stronger in the reduced NOGWD  
469 run (blue shading in the mesosphere in Fig. 9b) as there is no wave drag to counteract the strong  
470 diabatic cooling. The much weaker descent following the warming in response to the reduction in  
471 NOGWD is in agreement with McLandress et al. (2013), who find a similar response in the run  
472 without any NOGWD.

473 Because the PJO is more persistent in the reduced NOGWD run (i.e., the stratospheric zonal  
474 wind remains easterly for longer than in the control run), the ability of OGWs to propagate into the  
475 mesosphere is delayed in the reduced NOGWD run (Fig. 8c). This further contributes to the delay  
476 in the reformation of the stratopause. The stratopause begins to reform in the reduced NOGWD  
477 run only when sufficient parametrized and resolved wave drag is able to enter the mesosphere.  
478 The delay in the reformation of the stratopause was also observed by McLandress et al. (2013) in  
479 response to the removal of NOGWD.

480 The polar cap temperature in the lower stratosphere is colder in the reduced NOGWD run as the  
481 NOGWD induced downwelling is suppressed. Therefore, the westerlies in the lower stratosphere  
482 are stronger in the reduced NOGWD run following the SSW. This allows more planetary waves  
483 to enter the stratosphere and induce resolved wave downwelling that contributes to the longer  
484 persistence of the PJO. This can be seen in Figs. 8e and 8g, where the lower-stratospheric resolved  
485 wave drag and downwelling strength are stronger in the reduced NOGWD run.

486 Because the 2006 PJO event is not captured in the increased NOGWD run, instead the evolution  
487 of the SSW that started on 15 December 2006 in the increased NOGWD run is compared to the  
488 PJO event in the control run. Figure 9c-d shows the difference in the 50°N to 70°N zonal-mean  
489 zonal wind and the polar cap temperature between the 2006 PJO event in the control run and the

490 15 December 2006 SSW event in the increased NOGWD run. The zonal wind tendencies and  
491 the residual vertical velocity for the increased NOGWD run are shown in the right column of  
492 Fig. 8 (shading) together with the difference in these quantities between the increased NOGWD  
493 run and the control run (black and red contours). The response of the SSW life-cycle to increase  
494 in NOGWD is almost opposite to that in the reduced NOGWD case just discussed. The main  
495 difference is that the SSW life-cycle in the increased NOGWD run occurs lower down and that  
496 considerably less resolved wave drag is needed to initiate the SSW in the increased NOGWD run  
497 (compare Fig. 8e to Fig. 8f) due to the weakened vortex brought about by the NOGWD increase.  
498 In addition, OGWD plays little role in the reformation of the stratopause as OGWD decreases to  
499 compensate for the increase in NOGWD (see Fig. 8d). As the recovery from the SSW event is  
500 shorter in the increased NOGWD run, the vortex reforms allowing more planetary wave activity  
501 to enter the stratosphere and initiate another SSW in February.

#### 502 *b. SSWs in the free-running model*

503 Is the longer persistence of a SSW and a prolonged recovery of the stratopause following a  
504 SSW with reduction in NOGWD merely a feature of the 2006 PJO case study, or does it occur  
505 more generally following all SSW events in the model? To address this, composites of all SSWs  
506 from the free-running control run, reduced NOGWD run and increased NOGWD run are shown  
507 in Fig. 10 together with the ERA-Interim composites from 1979 to 2016. The composites are  
508 constructed as in McLandress and Shepherd (2009b). In the figure, 60°N zonal wind anomaly at  
509 10 hPa, and the polar cap temperature anomaly at different pressure levels, are shown. It is clear  
510 from the figure that the response of the 2006 PJO event to the reduction in NOGWD carries over to  
511 SSWs in general. Namely, as the NOGWD is reduced, the persistence of the SSW events lengthens  
512 (i.e., the wind and temperature anomalies last longer), mainly because the amplitude of the events

513 increase. Similarly, the reformation of the stratopause is delayed. An increase in NOGWD leads to  
514 opposite results. It should also be noted that the frequency of SSW events increases with increase  
515 in NOGWD: The frequency of SSWs for the reduced NOGWD run is 0.45/year; for the control  
516 run 0.6/year, and for the increased NOGWD run 0.9/year. This is expected as a weaker vortex in  
517 increased NOGWD runs is more amenable to wave breaking. Note that the control run captures  
518 the statistical behaviour of SSWs in the ERA-Interim remarkably well. The frequency of SSWs in  
519 the ERA-Interim reanalysis is 0.55/year.

## 520 **6. Summary and Conclusion**

521 The impact of parametrized nonorographic gravity wave drag on key aspects of polar strato-  
522 spheric dynamics was studied using the high-resolution IFS model. The focus was on the seasonal  
523 cycle of the residual mean meridional circulation, the SH vortex breakdown event, and NH SSWs.

524 Compared to the multi-model mean of Butchart et al. (2011), which was based on much lower-  
525 resolution models, the parametrized waves play a much smaller role in driving the tropical up-  
526 welling in the control IFS run (less than 7% everywhere in the stratosphere). The tropical up-  
527 welling is mostly influenced by resolved wave breaking in the lower stratosphere. However, the  
528 parametrized waves play a more important role in the winter polar cap downwelling, especially in  
529 the mid- to upper stratosphere and in particular over the SH winter pole. For example, at 10 hPa  
530 parametrized waves account for 40% of the polar cap downwelling (all NOGWs) in the SH and  
531 19% of the polar cap downwelling (14% OGWs, 5% NOGWs) in the NH. Therefore, the residual  
532 mean meridional circulation is strongly influenced by NOGWD in the SH.

533 In response to changes in NOGWD flux, the resolved wave drag shifts vertically leading to a  
534 counteraction of the NOGWD perturbation in the polar mid- to upper stratosphere and an amplifi-  
535 cation of the perturbation in the polar lower stratosphere. Due to the different partitioning of the

536 resolved and parameterized waves in driving the downwelling between the two hemispheres, the  
537 downwelling response in the total polar cap downwelling is different between the NH and the SH:  
538 The total downwelling increases with increase in NOGWD flux everywhere in the SH, whereas  
539 in the NH it decreases in the mid- to upper stratosphere but increases in the lower stratosphere.  
540 OGWD also counteracts NOGWD changes in the NH.

541 The maximum in the parameterized and the resolved wave downwelling over the polar cap is  
542 found to have a temporal offset; the parameterized waves dominate earlier in the winter and the  
543 resolved waves dominate later in the winter/early spring. This offset is larger in the SH. OGWs  
544 play no role in polar cap downwelling over the SH in the IFS. Due to the different seasonal cycles  
545 of the resolved and parametrized wave drags, the resolved and parameterized wave interaction  
546 does not occur on the Rossby wave propagation timescales when NOGWD is changed: During  
547 early winter, when the parameterized waves dominate the polar cap downwelling, the response is  
548 proportional to changes in NOGWD. In the late winter/spring, however, the downwelling response  
549 is found to be dominated by the resolved waves. Therefore the seasonal-mean perspective might  
550 paint a misleading picture of the resolved and parameterized wave interaction. In the NH, the  
551 interaction with OGWD further complicates the matter. Therefore, it is unlikely that the NOGWD  
552 and OGWD parameterizations can be tuned independently, a conclusion also drawn in McLandress  
553 et al. (2013). It is hence easier to tune the NOGWD parameterization in the SH.

554 Despite having a much smaller influence on the time-mean residual mean meridional circulation  
555 in the NH, NOGWD has a clear effect on the SSW composites in the free-running model and on  
556 the 2006 PJO event in the nudged model, in which the resolved wave fluxes entering the strato-  
557 sphere are constrained to the observations. In particular, reduction in NOGWD leads to a reduction  
558 in the SSW frequency, increase in the amplitude and persistence, and a delay in the recovery of  
559 the stratopause following a SSW event. While the composites of SSW events in the control run

560 agree well with ERA-Interim, this study illustrates that NOGWD flux exerts a strong influence on  
561 SSWs and might thus be a tunable parameter for obtaining a desired SSW behaviour in other mod-  
562 els. Moreover, the long-lived recovery period following SSWs represents a good opportunity to  
563 evaluate the accuracy of the model physics since the evolution is unaffected by chaotic variability.

564 Furthermore, increase in NOGWD is found to bring forward the final warming date in the SH  
565 as the weakened vortex in the stratosphere is more amenable to wave breaking. Given that many  
566 stratosphere-resolving chemistry-climate models have a late bias in the final warming date (Eyring  
567 et al. 2006; Butchart et al. 2011), it is possible that these models might be missing NOGWD.  
568 The final warming date in the control model climatology is, however, remarkably similar to the  
569 observed climatology and the IFS does not experience this late bias. Interestingly, Scheffler and  
570 Pulido (2015) find the opposite sign response in the final warming date in the stratosphere with  
571 changes to the NOGWD flux, with a delay in a final warming with increase in NOGWD flux. This  
572 occurs because the planetary wave breaking in the lower stratosphere is reduced with increased  
573 NOGW flux in their model, unlike in the IFS where the planetary wave forcing is markedly reduced  
574 in the upper stratosphere and mesosphere only.

575 As is shown here, the stratospheric circulation is profoundly influenced by NOGWD at  
576 TL255L137 resolution of the IFS, despite NOGWD mostly acting in the mesosphere and de-  
577 spite a greater role of the resolved gravity wave drag than in lower-resolution climate models.  
578 NOGWD exerts a strong influence on the polar night jet (in both hemispheres) and thus signifi-  
579 cantly alters the ability of resolved waves to influence stratospheric dynamics (i.e., the residual cir-  
580 culation, SSWs, and the final warming in the SH). As the resolution of climate models increases,  
581 parametrized orographic gravity wave drag becomes less important in the middle atmosphere.  
582 Given that the strong sponge applied at the model top is likely to unphysically damp the smaller-  
583 scale higher-frequency inertia-gravity waves, nonorographic gravity wave drag parametrization

584 will still be needed to substitute for this missing drag even in higher-resolution models with tops  
585 located in the mesosphere. Thus NOGWD becomes the only parametrization affecting the momen-  
586 tum budget in the middle atmosphere at high resolution. Therefore, it is important to understand  
587 circulation sensitivity to NOGWD in order to guide interpretation and tuning of general circulation  
588 models.

## 589 **Acknowledgments**

590 This article is based on Section 5 of the ECMWF technical memorandum of the authors  
591 (Polichtchouk et al. 2017). The authors thank Linus Magnusson and Tim Stockdale for help with  
592 setting up the IFS runs, Peter Hitchcock for providing gridded MLS temperature data, Nick Byrne  
593 for helpful discussions, and the three anonymous reviewers for their helpful comments. IP and  
594 TGS are supported by the “Understanding the atmospheric circulation response to climate change”  
595 (ACRCC, ERC Advanced Grant, number 339390) project.

## 596 **References**

- 597 Andrews, D. G., J. R. Holton, and C. B. Leovy, 1987: *Middle atmosphere dynamics*. Academic  
598 Press.
- 599 Baldwin, M. P., and T. J. Dunkerton, 2001: Stratospheric harbingers of anomalous weather  
600 regimes. *Science*, **294**, 581–584.
- 601 Black, R. X., and B. A. McDaniel, 2007: Interannual variability in the southern hemisphere cir-  
602 culation organized by stratospheric final warming events. *Journal of the Atmospheric Sciences*,  
603 **64**, 2968–2974.
- 604 Butchart, N., 2014: The Brewer-Dobson circulation. *Reviews of Geophysics*, **52**, 157–184.

- 605 Butchart, N., and Coauthors, 2011: Multimodel climate and variability of the stratosphere. *Journal*  
606 *of Geophysical Research: Atmospheres*, **116**, doi:10.1029/2010JD014995, d05102.
- 607 Charney, J. G., and P. G. Drazin, 1961: Propagation of planetary-scale disturbances from the lower  
608 into the upper atmosphere. *Journal of Geophysical Research*, **66**, 83–109.
- 609 Cohen, N. Y., E. P. Gerber, and O. Bühler, 2013: Compensation between resolved and unresolved  
610 wave driving in the stratosphere: Implications for downward control. *Journal of the Atmospheric*  
611 *Sciences*, **70**, 3780–3798.
- 612 Cohen, N. Y., E. P. Gerber, and O. Bühler, 2014: What drives the Brewer–Dobson circulation?  
613 *Journal of the Atmospheric Sciences*, **71**, 3837–3855.
- 614 Dee, D., and Coauthors, 2011: The ERA-Interim reanalysis: Configuration and performance of the  
615 data assimilation system. *Quarterly Journal of the Royal Meteorological Society*, **137**, 553–597.
- 616 Douville, H., 2009: Stratospheric polar vortex influence on northern hemisphere winter climate  
617 variability. *Geophysical Research Letters*, **36**, doi:10.1029/2009GL039334, 118703.
- 618 ECMWF, 2016: IFS documentation. CY43R1. [http://www.ecmwf.int/en/forecasts/documentation-](http://www.ecmwf.int/en/forecasts/documentation-and-support/changes-ecmwf-model/ifs-documentation)  
619 [and-support/changes-ecmwf-model/ifs-documentation](http://www.ecmwf.int/en/forecasts/documentation-and-support/changes-ecmwf-model/ifs-documentation).
- 620 Eyring, V., and Coauthors, 2006: Assessment of temperature, trace species, and ozone in  
621 chemistry-climate model simulations of the recent past. *Journal of Geophysical Research: At-*  
622 *mospheres*, **111**.
- 623 Fritts, D. C., and M. J. Alexander, 2003: Gravity wave dynamics and effects in the middle atmo-  
624 sphere. *Reviews of Geophysics*, **41**, doi:10.1029/2001RG000106, 1003.

625 Haynes, P. H., M. E. McIntyre, C. J. Marks, T. G. Shepherd, and K. P. Shine, 1991: On the  
626 “downward control” of extratropical diabatic circulations by eddy-induced mean zonal forces.  
627 *Journal of the Atmospheric Sciences*, **48**, 651–678.

628 Hitchcock, P., and T. G. Shepherd, 2013: Zonal-mean dynamics of extended recoveries from  
629 stratospheric sudden warmings. *Journal of the Atmospheric Sciences*, **70**, 688–707.

630 Hitchcock, P., T. G. Shepherd, and G. L. Manney, 2013: Statistical characterization of Arctic  
631 polar-night jet oscillation events. *Journal of Climate*, **26**, 2096–2116.

632 Hitchcock, P., and I. R. Simpson, 2014: The downward influence of stratospheric sudden warm-  
633 ings. *Journal of the Atmospheric Sciences*, **71**, 3856–3876.

634 Holton, J., 1990: On the global exchange of mass between the stratosphere and troposphere.  
635 *Journal of the Atmospheric Sciences*, **47**, 392–395.

636 Kushner, P. J., and L. M. Polvani, 2004: Stratosphere–troposphere coupling in a relatively simple  
637 AGCM: The role of eddies. *Journal of Climate*, **17**, 629–639.

638 Limpasuvan, V., J. H. Richter, Y. J. Orsolini, F. Stordal, and O.-K. Kvissel, 2012: The roles of  
639 planetary and gravity waves during a major stratospheric sudden warming as characterized in  
640 WACCM. *Journal of Atmospheric and Solar-Terrestrial Physics*, **78**, 84–98.

641 Livesey, N. J., and Coauthors, 2011: Earth Observing System (EOS) Aura Microwave Limb  
642 Sounder MLS version 3.3 level 2 data quality and description document. *JPL D-33509*.

643 Lott, F., and M. J. Miller, 1997: A new subgrid-scale orographic drag parametrization: Its formu-  
644 lation and testing. *Quarterly Journal of the Royal Meteorological Society*, **123**, 101–127.

645 McLandress, C., J. F. Scinocca, T. G. Shepherd, M. C. Reader, and G. L. Manney, 2013: Dynam-  
646 ical control of the mesosphere by orographic and nonorographic gravity wave drag during the



647 extended northern winters of 2006 and 2009. *Journal of the Atmospheric Sciences*, **70**, 2152–  
648 2169.

649 McLandress, C., and T. G. Shepherd, 2009a: Simulated anthropogenic changes in the Brewer–  
650 Dobson circulation, including its extension to high latitudes. *Journal of Climate*, **22**, 1516–1540,  
651 doi:10.1175/2008JCLI2679.1.

652 McLandress, C., and T. G. Shepherd, 2009b: Impact of climate change on stratospheric sudden  
653 warmings as simulated by the Canadian Middle Atmosphere Model. *Journal of Climate*, **22**,  
654 5449–5463, doi:10.1175/2009JCLI3069.1.

655 McLandress, C., T. G. Shepherd, S. Polavarapu, and S. R. Beagley, 2012: Is missing orographic  
656 gravity wave drag near 60°S the cause of the stratospheric zonal wind biases in chemistry–  
657 climate models? *Journal of the Atmospheric Sciences*, **69**, 802–818.

658 Orr, A., P. Bechtold, J. Scinocca, M. Ern, and M. Janiskova, 2010: Improved middle atmosphere  
659 climate and forecasts in the ECMWF model through a nonorographic gravity wave drag param-  
660 eterization. *Journal of Climate*, **23**, 5905–5926.

661 Plougonven, R., and F. Zhang, 2014: Internal gravity waves from atmospheric jets and fronts.  
662 *Reviews of Geophysics*, **52**, 33–76, doi:10.1002/2012RG000419.

663 Polavarapu, S., T. G. Shepherd, Y. Rochon, and S. Ren, 2005: Some challenges of middle atmo-  
664 sphere data assimilation. *Quarterly Journal of the Royal Meteorological Society*, **131**, 3513–  
665 3527, doi:10.1256/qj.05.87.

666 Polichtchouk, I., R. Hogan, T. Shepherd, P. Bechtold, T. Stockdale, S. Malardel, S.-J. Lock, and  
667 L. Magnusson, 2017: What controls the middle atmosphere circulation in the IFS? Tech. Rep.  
668 809, ECMWF.

- 669 Pulido, M., and J. Thuburn, 2008: The seasonal cycle of gravity wave drag in the middle atmo-  
670 sphere. *Journal of Climate*, **21**, 4664–4679, doi:10.1175/2008JCLI2006.1.
- 671 Quintanar, A. I., and C. R. Mechoso, 1995: Quasi-stationary waves in the southern hemisphere.  
672 part i: Observational data. *Journal of Climate*, **8**, 2659–2672.
- 673 Randel, W. J., 1988: The seasonal evolution of planetary waves in the southern hemisphere strato-  
674 sphere and troposphere. *Quarterly Journal of the Royal Meteorological Society*, **114**, 1385–  
675 1409.
- 676 Randel, W. J., R. Garcia, and F. Wu, 2008: Dynamical balances and tropical stratospheric up-  
677 welling. *Journal of the Atmospheric Sciences*, **65**, 3584–3595.
- 678 Ren, S., S. M. Polavarapu, and T. G. Shepherd, 2008: Vertical propagation of information in  
679 a middle atmosphere data assimilation system by gravity-wave drag feedbacks. *Geophysical*  
680 *Research Letters*, **35**, doi:10.1029/2007GL032699, 106804.
- 681 Sakazaki, T., T. Sasaki, M. Shiotani, Y. Tomikawa, and D. Kinnison, 2015: Zonally uniform tidal  
682 oscillations in the tropical stratosphere. *Geophysical Research Letters*, **42**, 9553–9560.
- 683 Scheffler, G., and M. Pulido, 2015: Compensation between resolved and unresolved wave drag  
684 in the stratospheric final warmings of the southern hemisphere. *Journal of the Atmospheric*  
685 *Sciences*, **72**, 4393–4411.
- 686 Scheffler, G., and M. Pulido, 2017: Estimation of gravity-wave parameters to alleviate the delay  
687 in the Antarctic vortex breakup in general circulation models. *Quarterly Journal of the Royal*  
688 *Meteorological Society*, **143**, 2157–2167, doi:10.1002/qj.3074.
- 689 Scinocca, J. F., 2003: An accurate spectral nonorographic gravity wave drag parameterization for  
690 general circulation models. *Journal of the Atmospheric Sciences*, **60**, 667–682.

- 691 Seviour, W. J., N. Butchart, and S. C. Hardiman, 2012: The Brewer–Dobson circulation inferred  
692 from ERA-Interim. *Quarterly Journal of the Royal Meteorological Society*, **138**, 878–888.
- 693 Shaw, T. A., M. Sigmond, T. G. Shepherd, and J. F. Scinocca, 2009: Sensitivity of simulated cli-  
694 mate to conservation of momentum in gravity wave drag parameterization. *Journal of Climate*,  
695 **22**, 2726–2742, doi:10.1175/2009JCLI2688.1.
- 696 Shepherd, T. G., 2000: The middle atmosphere. *Journal of Atmospheric and Solar-Terrestrial*  
697 *Physics*, **62**, 1587–1601.
- 698 Sigmond, M., J. F. Scinocca, V. V. Kharin, and T. G. Shepherd, 2013: Enhanced seasonal forecast  
699 skill following stratospheric sudden warmings. *Nature Geoscience*, **6**, 98–102.
- 700 Sigmond, M., and T. G. Shepherd, 2014: Compensation between resolved wave driving and pa-  
701 rameterized orographic gravity wave driving of the Brewer-Dobson circulation and its response  
702 to climate change. *Journal of Climate*, **27**, 5601–5610.
- 703 Siskind, D. E., S. D. Eckermann, J. P. McCormack, L. Coy, K. W. Hoppel, and N. L. Baker, 2010:  
704 Case studies of the mesospheric response to recent minor, major, and extended stratospheric  
705 warmings. *Journal of Geophysical Research: Atmospheres*, **115**, doi:10.1029/2010JD014114,  
706 d00N03.
- 707 Tomikawa, Y., K. Sato, S. Watanabe, Y. Kawatani, K. Miyazaki, and M. Takahashi, 2012: Growth  
708 of planetary waves and the formation of an elevated stratopause after a major stratospheric  
709 sudden warming in a T213L256 GCM. *Journal of Geophysical Research: Atmospheres*, **117**,  
710 doi:10.1029/2011JD017243, d16101.

711 **LIST OF TABLES**

712 **Table 1.** Resolved and parametrized (OGWD and NOGWD) wave contribution (in % of  
713 the total) to the annual-mean tropical mass flux and extended winter (Mar-Nov  
714 for the SH, and Oct-May for the NH) polar cap downward mass flux for the control,  
715 reduced NOGWD and increased NOGWD runs at 10 hPa and at 70 hPa.  
716 Positive percentage denotes tropical upwelling and polar cap downwelling and  
717 negative percentage denotes tropical downwelling and polar cap upwelling. . . . 35

718 TABLE 1. Resolved and parametrized (OGWD and NOGWD) wave contribution (in % of the total) to the  
719 annual-mean tropical mass flux and extended winter (Mar-Nov for the SH, and Oct-May for the NH) polar cap  
720 downward mass flux for the control, reduced NOGWD and increased NOGWD runs at 10 hPa and at 70 hPa.  
721 Positive percentage denotes tropical upwelling and polar cap downwelling and negative percentage denotes  
722 tropical downwelling and polar cap upwelling.

Experiment	Region	Pressure [hPa]	Parametrized wave drag [%]			Resolved wave drag [%]	Mass flux $\times 10^8$ [kg/s]
			OGWD	NOGWD	All		
Control	Annual-mean upwelling	10	2.4	-2.4	0	100	15.5
		70	5	2	7	93	58.1
	NH polar cap downwelling	10	14	5	19	81	5.7
		70	7	0	7	93	22.2
	SH polar cap downwelling	10	0	40.6	40.6	59	5.8
		70	0	19	19	81	15
Reduced NOGWD	Annual-mean upwelling	10	2.5	-3	-0.5	100.5	16.1
		70	5	-3	2	98	57.1
	NH polar cap downwelling	10	14	-9	5	95	6.2
		70	8	-6	2	98	20.7
	SH polar cap downwelling	10	0	12	12	88	5.4
		70	0	6	6	94	13.5
Increased NOGWD	Annual-mean upwelling	10	4	6	10	90	11.8
		70	4	16	20	80	57.4
	NH polar cap downwelling	10	7.5	38.5	46	54	5.2
		70	5	14	19	81	23.2
	SH polar cap downwelling	10	0	88	88	12	6.7
		70	0	45	45	55	19.3

723

## LIST OF FIGURES

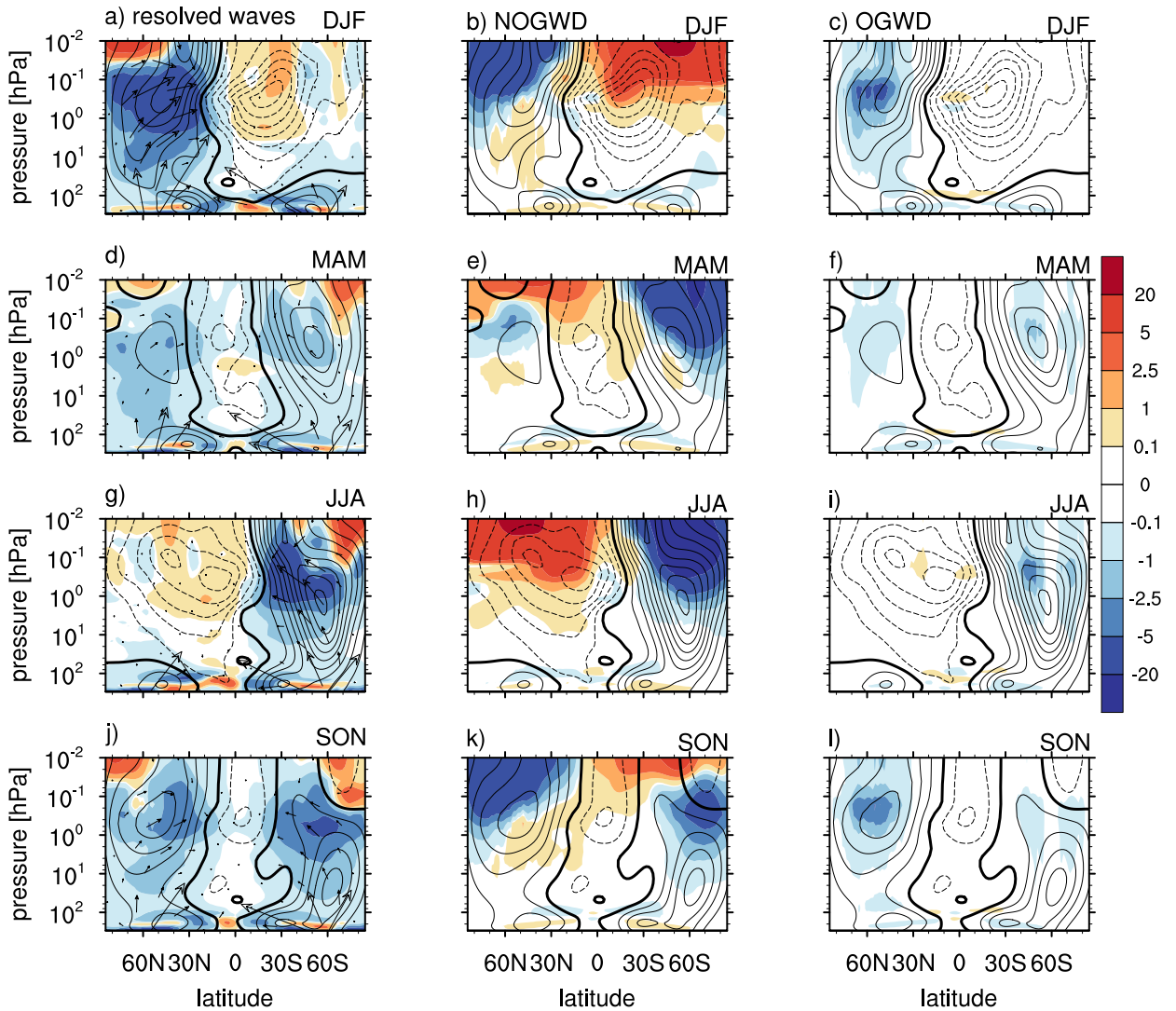
- 724 **Fig. 1.** Latitude-pressure cross sections of zonal-mean zonal wind tendencies (in  $\text{m s}^{-1} \text{ day}^{-1}$ ) for  
 725 the control run in the middle atmosphere: (a-c) December-February, (d-f) March-May, (g-i)  
 726 June-August, and (j-l) September-November. Resolved wave tendency is shown in left col-  
 727 umn, NOGWD tendency is shown in middle column, and OGWD tendency in right column.  
 728 Negative values are in blue and positive in red. The EP flux vectors are represented by the  
 729 arrows (in  $\text{m}^3 \text{ s}^{-2}$ ). Note the non-linear contour interval for tendencies. The zonal-mean  
 730 zonal wind in  $\text{m s}^{-1}$  is shown in black contours (contour interval  $10 \text{ m s}^{-1}$ ), negative con-  
 731 tours are dashed and the zero contour is drawn with double thickness. Negative tendencies  
 732 denote westward momentum deposition and positive eastward momentum deposition. . . . . 38
- 733 **Fig. 2.** (a) Annual-mean upward mass flux over the tropics and extended winter downward mass  
 734 flux over (b) the NH (Oct-May) and (c) the SH (March-Nov) polar cap (poleward of  $60^\circ\text{N/S}$ )  
 735 for the control run. The solid lines show the total downward-control mass flux and the  
 736 dashed lines show the parametrized wave contribution. (d-f) Difference in the mass fluxes  
 737 between increased and reduced NOGWD runs. The thickened lines in (d-f) show regions  
 738 where the response is significant at the 95% level by the Student-t test on the means. Mass  
 739 flux calculated from the DC streamfunction is shown in blue, from the parametrized wave  
 740 contribution to the DC streamfunction in black and from the resolved wave contribution to  
 741 the DC streamfunction in red. . . . . 39
- 742 **Fig. 3.** (a-b) Latitude-pressure cross sections of the resolved wave drag difference (in shading, units  
 743  $\text{m s}^{-1} \text{ day}^{-1}$ ) between the increased and reduced NOGWD runs for the extended (a) NH  
 744 (Oct-May) and (b) SH (March-November) winters. The EP flux vectors are shown by the  
 745 arrows ( $\text{m}^3 \text{ s}^{-2}$ ). The zonal-mean zonal wind difference ( $\text{m s}^{-1}$ ) is shown in black contours  
 746 (contour interval  $10 \text{ m s}^{-1}$ ), negative contours are dashed and the zero contour is drawn with  
 747 double thickness. (c-d) The EP flux budget (in  $\times 10^{16} \text{ N m}$ ) for the extended (c) NH and (d)  
 748 SH winters for the reduced NOGWD (in green) and increased NOGWD run (in red) for the  
 749 two boxes (see text). The positive numbers inside the boxes show the net resolved wave  
 750 convergence (i.e., the wave breaking). The vertical arrows represent vertical EP fluxes and  
 751 the horizontal arrows represent horizontal EP fluxes. . . . . 40
- 752 **Fig. 4.** Seasonal cycle of the downward-control residual vertical velocity  $\bar{w}_{DC}^*$  (thick lines, top pan-  
 753 els in each figure), split into its parameterized wave (dashed lines, bottom panels in each  
 754 figure) and resolved wave (thin solid lines, bottom panels in each figure) contributions av-  
 755 eraged over the (a,c) NH and (b,d) SH polar cap (between  $60\text{-}85^\circ\text{N/S}$ ) at (a,b) 10 hPa and  
 756 (c,d) 70 hPa, respectively. Black lines denote the control run, red lines reduced NOGWD  
 757 run, and blue lines increased NOGWD run, respectively. Note that the time-axis has been  
 758 shifted by six months in (a,c) for clarity. . . . . 41
- 759 **Fig. 5.** Seasonal cycle of the difference in the downward-control residual vertical velocity  $\bar{w}_{DC}^*$   
 760 (thick black lines) between the increased and reduced NOGWD runs, split into its parame-  
 761 terized wave (dash-dotted blue lines) and resolved wave (dotted black lines) contributions.  
 762 The NOGWD change is shown in solid green and the OGWD change is shown in dashed  
 763 red.  $\bar{w}_{DC}^*$  response averaged over the (a,c) NH and (b,d) SH polar cap at (a,b) 10 hPa and at  
 764 (c,d) 70 hPa. . . . . 42
- 765 **Fig. 6.** Average of the final warming dates in the SH for the control run (solid black), the reduced  
 766 NOGWD run (long-dashed red) and the increased NOGWD run (short-dashed blue). The  
 767 average of the ERA-Interim final warming dates between 2004 and 2015 is shown in thick  
 768 dot-dashed black contour. The shading shows the  $2\text{-}\sigma$  interval for the increased and reduced  
 769 NOGWD runs only. . . . . 43

770 **Fig. 7.** Pressure-time cross sections of the zonal-mean zonal wind averaged from 50°N to 70°N  
771 (left column) and the polar-cap average (from 70°N to 90°N) zonal-mean temperature (right  
772 column) for the 2006 PJO event. (a-b) MLS observations (zonal wind computed using  
773 gradient-wind balance); (c-d) control nudged run; (e-f) reduced NOGWD nudged run; and  
774 (g-h) increased NOGWD nudged run. For the simulations, the ensemble mean is shown.  
775 The vertical lines mark the central date of SSWs. (i) Zonal-mean zonal wind at 60°N and at  
776 10 hPa for all ensemble members in the control run (black lines) and the MLS observations  
777 (thick red line). . . . . 44

778 **Fig. 8.** Shading: Pressure-time cross sections of the ensemble-mean polar-cap average (a-b)  
779 NOGWD tendency, (c-d) OGWD tendency, (e-f) resolved wave tendency, and (g-f) residual  
780 vertical velocity  $\bar{w}^*$  for the control run (left column) and the increased NOGWD run (right  
781 column), during the life-cycle of the 2006 PJO event. Dashed black (negative) and solid red  
782 (positive) contours: Response in tendencies and  $\bar{w}^*$  to reducing NOGWD (left column) and  
783 increasing NOGWD (right column) (contour interval is 4 m s<sup>-1</sup> day<sup>-1</sup> in a-d, 2 m s<sup>-1</sup> day<sup>-1</sup>  
784 in e-f, and 1 mm s<sup>-1</sup> in g-h). Time zero represents the central dates of SSWs: 6 January  
785 2006 for the control run, 9 January 2006 for the reduced NOGWD run and 15 December  
786 2005 for the increased NOGWD run. The resolved wave tendency and  $\bar{w}^*$  are smoothed by  
787 taking a 10-day running mean. Note that the pressure range is from 70 to 0.01 hPa. . . . . 45

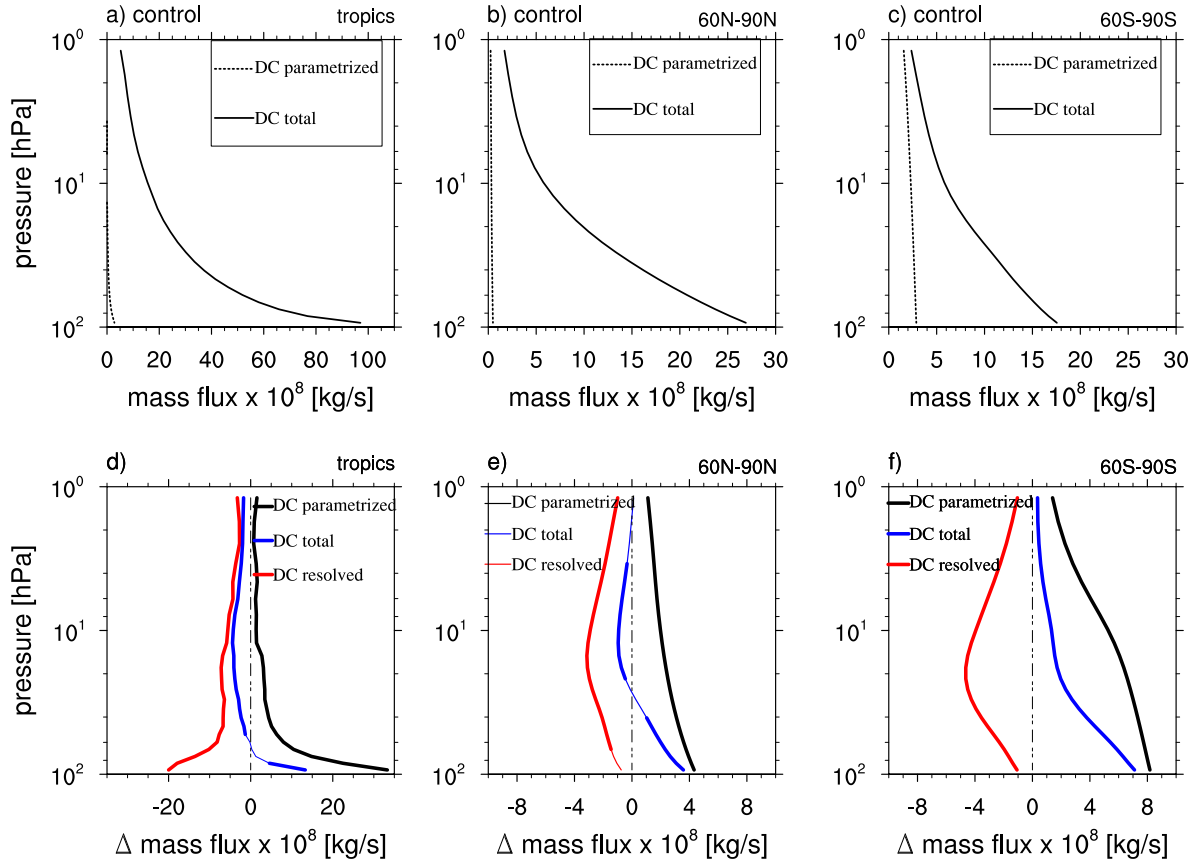
788 **Fig. 9.** Difference in (a,c) the 50°N to 70°N zonal-mean zonal wind (in m s<sup>-1</sup>) and (b,d) the polar  
789 cap average zonal-mean temperature (in K) between (a-b) the reduced NOGWD run and the  
790 control run and (c-d) the increased NOGWD run and the control run. . . . . 46

791 **Fig. 10.** Composites of all SSWs for the control run (solid black), reduced NOGWD run (dot-dashed  
792 red) and increased NOGWD run (dashed blue) with the free-running model. Thick black  
793 line shows composites of SSWs from the ERA-Interim reanalysis between 1979 and 2016:  
794 (a) Zonal-mean zonal wind anomaly at 60°N and 10 hPa (in m s<sup>-1</sup>); Polar-cap average (from  
795 70°N to 90°N) zonal-mean temperature anomalies (in K) at (b) 1 hPa; (c) 10 hPa; and (d)  
796 50 hPa. . . . . 47

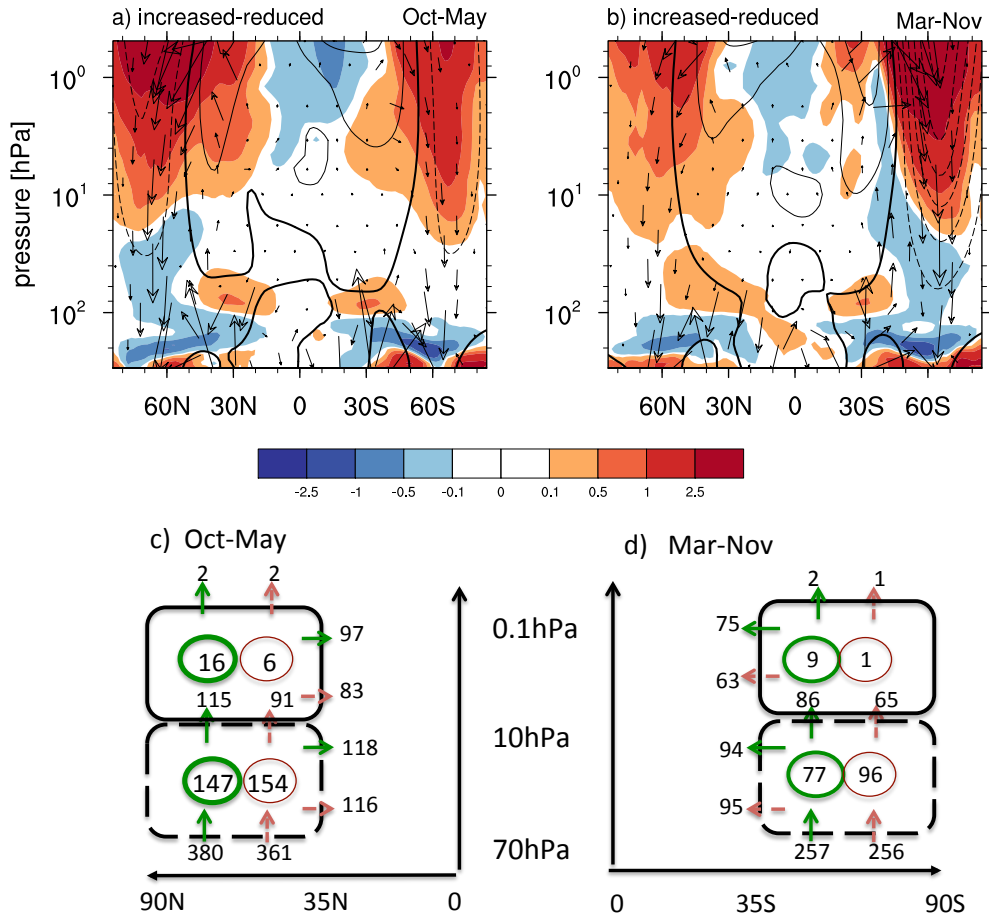


797 FIG. 1. Latitude-pressure cross sections of zonal-mean zonal wind tendencies (in  $\text{m s}^{-1} \text{ day}^{-1}$ ) for the con-  
 798 trol run in the middle atmosphere: (a-c) December-February, (d-f) March-May, (g-i) June-August, and (j-l)  
 799 September-November. Resolved wave tendency is shown in left column, NOGWD tendency is shown in middle  
 800 column, and OGWD tendency in right column. Negative values are in blue and positive in red. The EP flux  
 801 vectors are represented by the arrows (in  $\text{m}^3 \text{ s}^{-2}$ ). Note the non-linear contour interval for tendencies. The  
 802 zonal-mean zonal wind in  $\text{m s}^{-1}$  is shown in black contours (contour interval  $10 \text{ m s}^{-1}$ ), negative contours are  
 803 dashed and the zero contour is drawn with double thickness. Negative tendencies denote westward momentum  
 804 deposition and positive eastward momentum deposition.

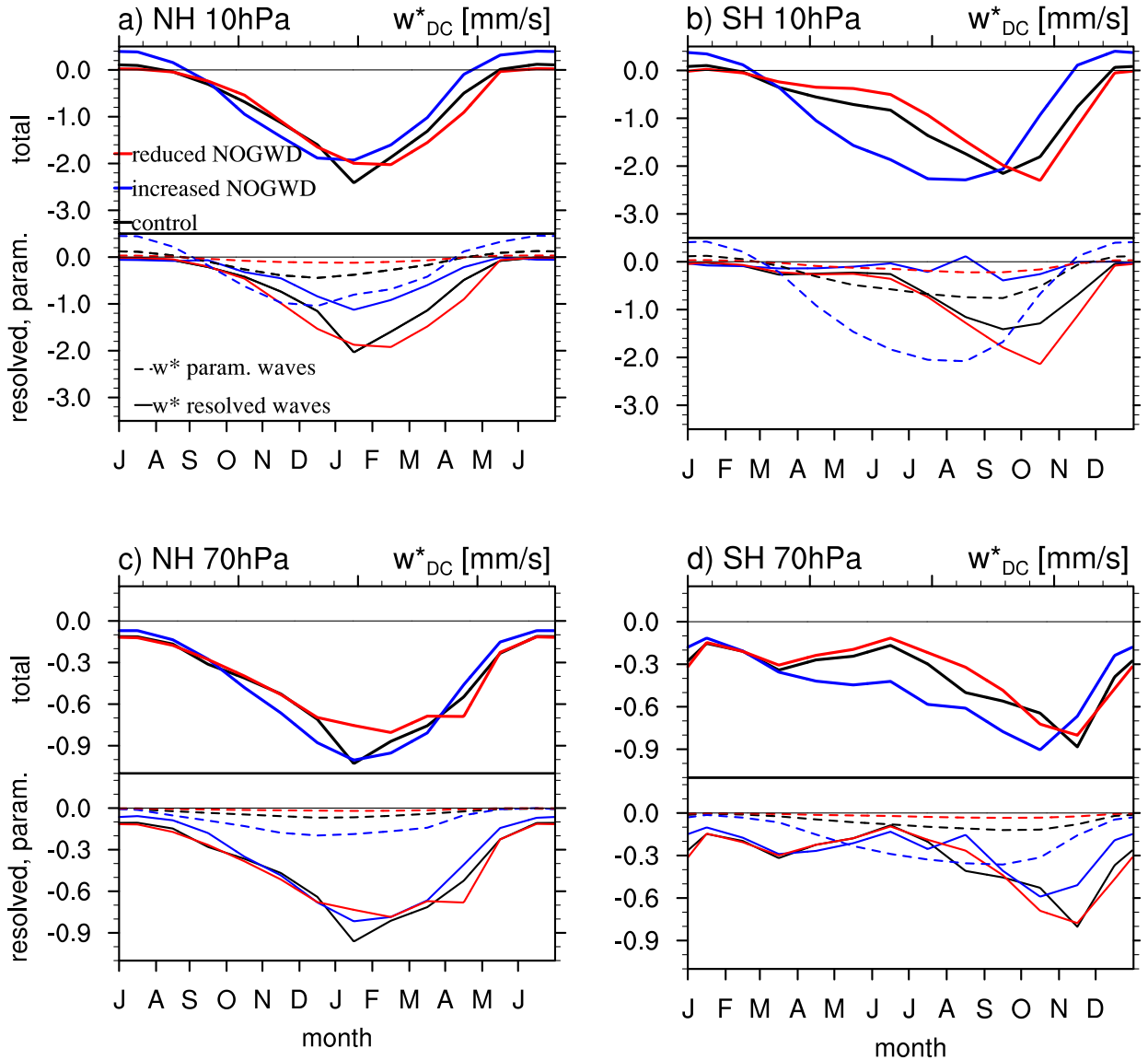




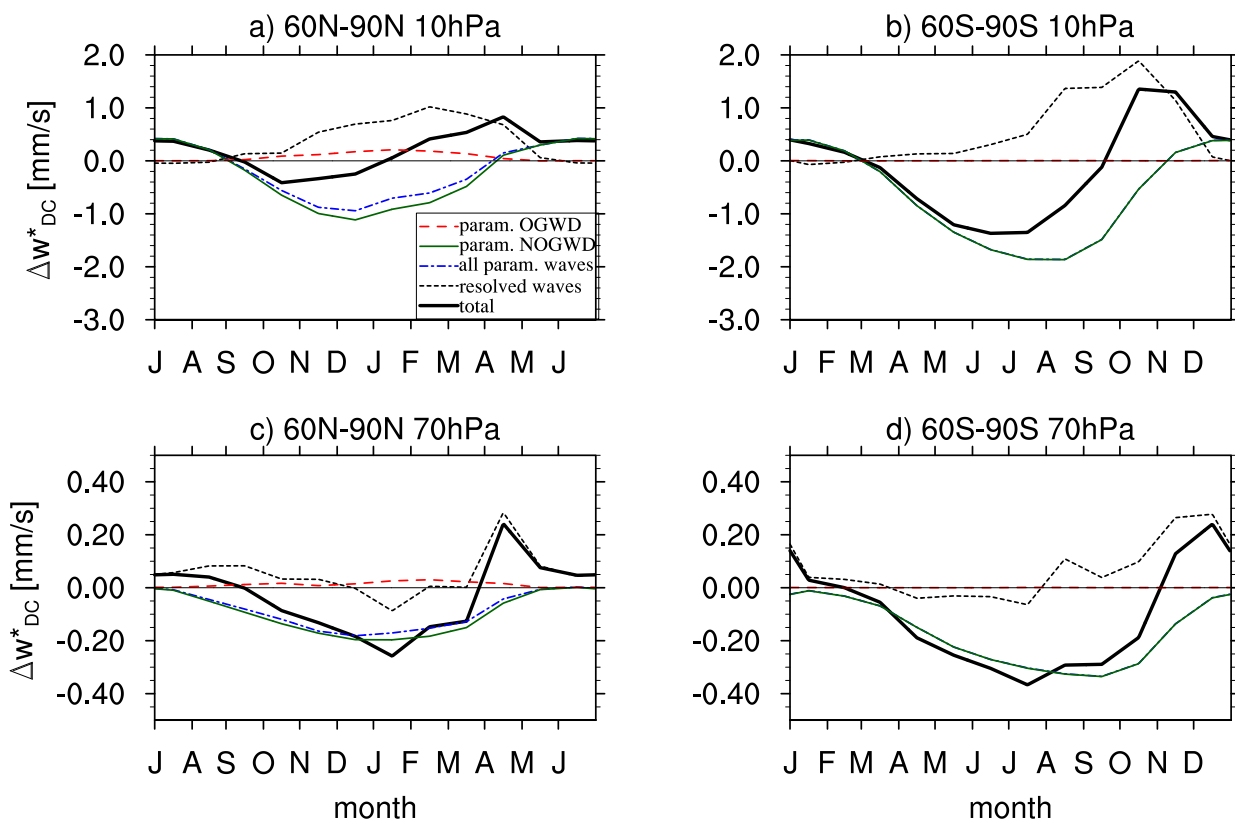
805 FIG. 2. (a) Annual-mean upward mass flux over the tropics and extended winter downward mass flux over (b)  
 806 the NH (Oct-May) and (c) the SH (March-Nov) polar cap (poleward of  $60^\circ$ N/S) for the control run. The solid  
 807 lines show the total downward-control mass flux and the dashed lines show the parametrized wave contribution.  
 808 (d-f) Difference in the mass fluxes between increased and reduced NOGWD runs. The thickened lines in (d-f)  
 809 show regions where the response is significant at the 95% level by the Student-t test on the means. Mass flux  
 810 calculated from the DC streamfunction is shown in blue, from the parametrized wave contribution to the DC  
 811 streamfunction in black and from the resolved wave contribution to the DC streamfunction in red.



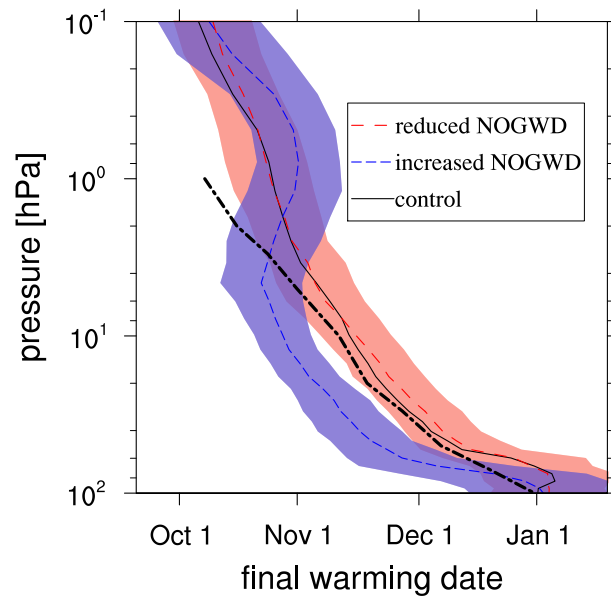
812 FIG. 3. (a-b) Latitude-pressure cross sections of the resolved wave drag difference (in shading, units  
 813  $\text{m s}^{-1} \text{ day}^{-1}$ ) between the increased and reduced NOGWD runs for the extended (a) NH (Oct-May) and (b)  
 814 SH (March-November) winters. The EP flux vectors are shown by the arrows ( $\text{m}^3 \text{ s}^{-2}$ ). The zonal-mean zonal  
 815 wind difference ( $\text{m s}^{-1}$ ) is shown in black contours (contour interval  $10 \text{ m s}^{-1}$ ), negative contours are dashed  
 816 and the zero contour is drawn with double thickness. (c-d) The EP flux budget (in  $\times 10^{16} \text{ N m}$ ) for the extended  
 817 (c) NH and (d) SH winters for the reduced NOGWD (in green) and increased NOGWD run (in red) for the two  
 818 boxes (see text). The positive numbers inside the boxes show the net resolved wave convergence (i.e., the wave  
 819 breaking). The vertical arrows represent vertical EP fluxes and the horizontal arrows represent horizontal EP  
 820 fluxes.



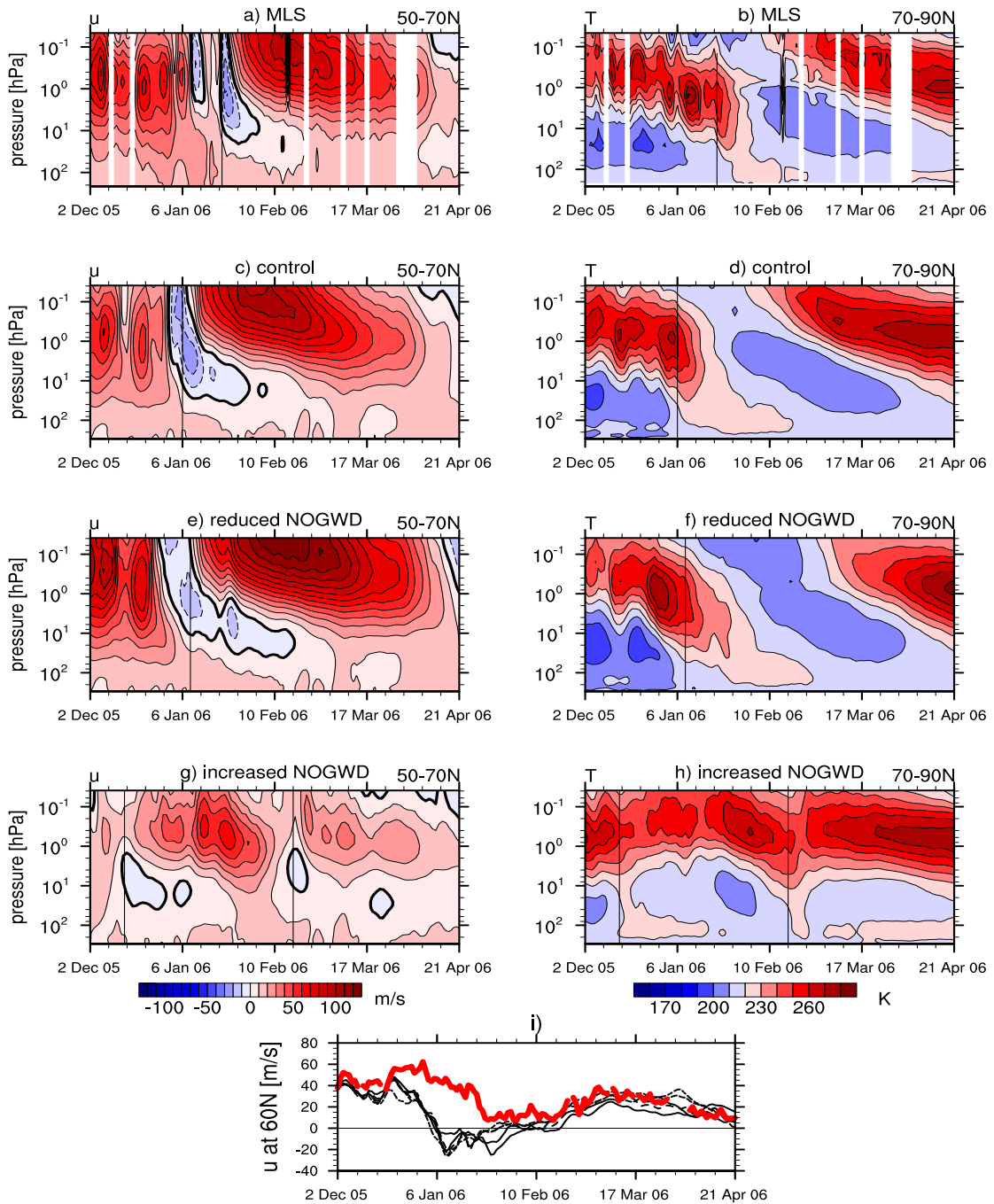
821 FIG. 4. Seasonal cycle of the downward-control residual vertical velocity  $\bar{w}_{DC}^*$  (thick lines, top panels in  
 822 each figure), split into its parameterized wave (dashed lines, bottom panels in each figure) and resolved wave  
 823 (thin solid lines, bottom panels in each figure) contributions averaged over the (a,c) NH and (b,d) SH polar cap  
 824 (between 60-85°N/S) at (a,b) 10 hPa and (c,d) 70 hPa, respectively. Black lines denote the control run, red lines  
 825 reduced NOGWD run, and blue lines increased NOGWD run, respectively. Note that the time-axis has been  
 826 shifted by six months in (a,c) for clarity.



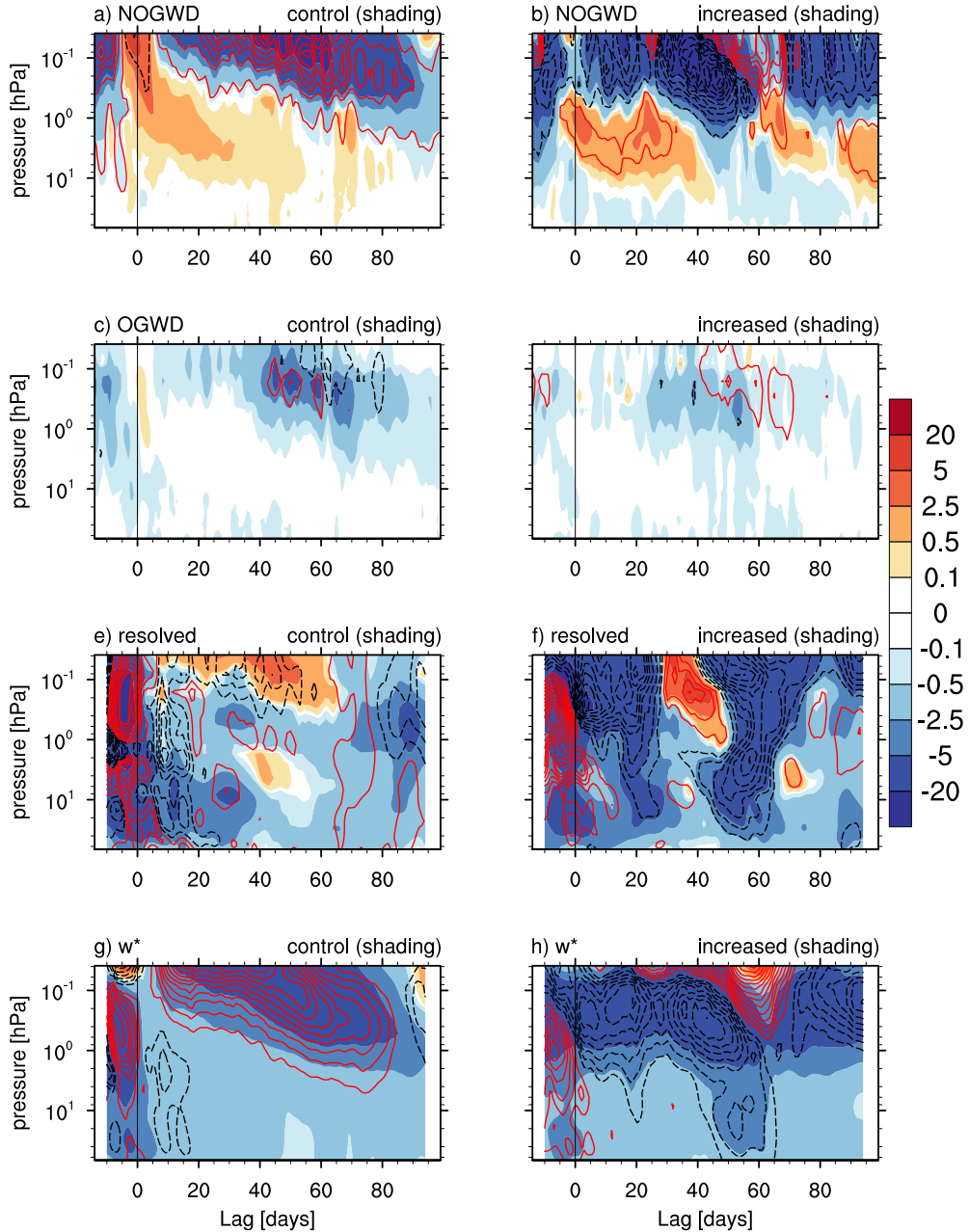
827 FIG. 5. Seasonal cycle of the difference in the downward-control residual vertical velocity  $\bar{w}_{DC}^*$  (thick black  
 828 lines) between the increased and reduced NOGWD runs, split into its parameterized wave (dash-dotted blue  
 829 lines) and resolved wave (dotted black lines) contributions. The NOGWD change is shown in solid green and  
 830 the OGWD change is shown in dashed red.  $\bar{w}_{DC}^*$  response averaged over the (a,c) NH and (b,d) SH polar cap at  
 831 (a,b) 10 hPa and at (c,d) 70 hPa.



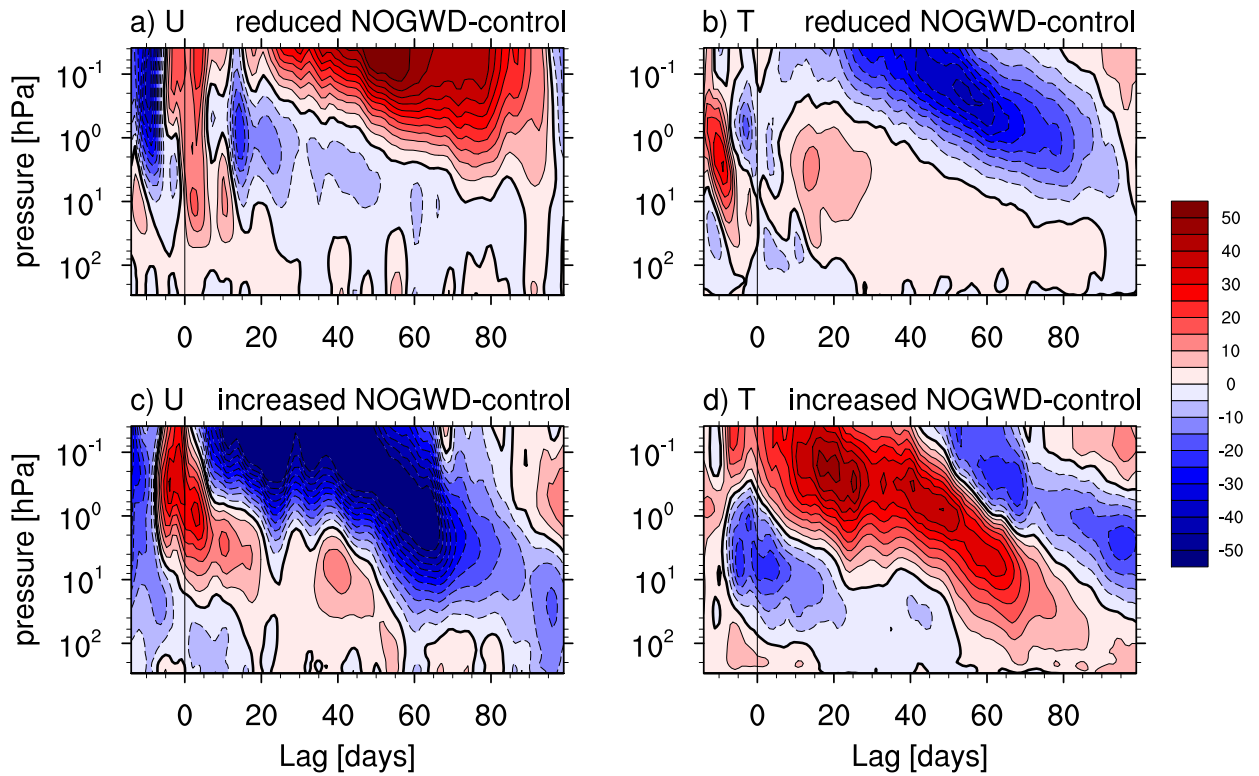
832 FIG. 6. Average of the final warming dates in the SH for the control run (solid black), the reduced NOGWD  
 833 run (long-dashed red) and the increased NOGWD run (short-dashed blue). The average of the ERA-Interim final  
 834 warming dates between 2004 and 2015 is shown in thick dot-dashed black contour. The shading shows the  $2\text{-}\sigma$   
 835 interval for the increased and reduced NOGWD runs only.



836 FIG. 7. Pressure-time cross sections of the zonal-mean zonal wind averaged from 50°N to 70°N (left column)  
 837 and the polar-cap average (from 70°N to 90°N) zonal-mean temperature (right column) for the 2006 PJO event.  
 838 (a-b) MLS observations (zonal wind computed using gradient-wind balance); (c-d) control nudged run; (e-f)  
 839 reduced NOGWD nudged run; and (g-h) increased NOGWD nudged run. For the simulations, the ensemble  
 840 mean is shown. The vertical lines mark the central date of SSWs. (i) Zonal-mean zonal wind at 60°N and at  
 841 10 hPa for all ensemble members in the control run (black lines) and the MLS observations (thick red line).

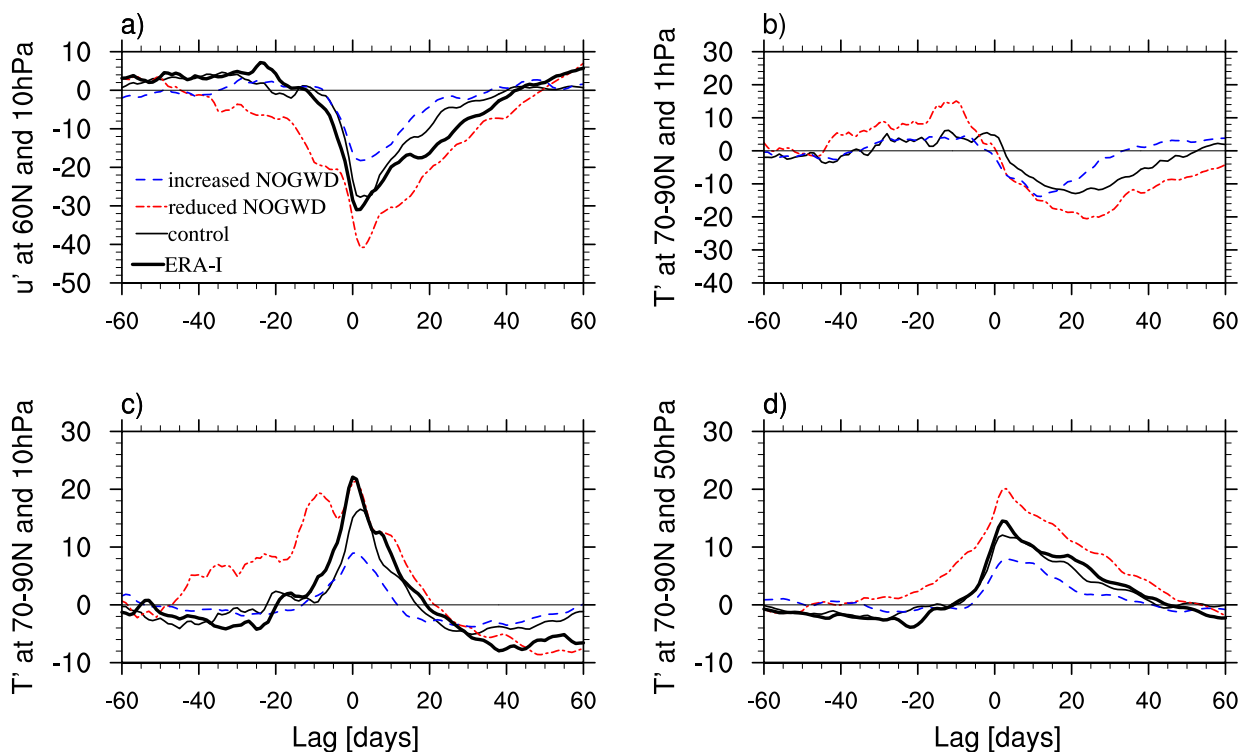


842 FIG. 8. Shading: Pressure-time cross sections of the ensemble-mean polar-cap average (a-b) NOGWD ten-  
 843 dency, (c-d) OGWD tendency, (e-f) resolved wave tendency, and (g-f) residual vertical velocity  $\bar{w}^*$  for the control  
 844 run (left column) and the increased NOGWD run (right column), during the life-cycle of the 2006 PJO event.  
 845 Dashed black (negative) and solid red (positive) contours: Response in tendencies and  $\bar{w}^*$  to reducing NOGWD  
 846 (left column) and increasing NOGWD (right column) (contour interval is  $4 \text{ m s}^{-1} \text{ day}^{-1}$  in a-d,  $2 \text{ m s}^{-1} \text{ day}^{-1}$   
 847 in e-f, and  $1 \text{ mm s}^{-1}$  in g-h). Time zero represents the central dates of SSWs: 6 January 2006 for the control  
 848 run, 9 January 2006 for the reduced NOGWD run and 15 December 2005 for the increased NOGWD run. The  
 849 resolved wave tendency and  $\bar{w}^*$  are smoothed by taking a 10-day running mean. Note that the pressure range is  
 850 from 70 to 0.01 hPa.



851 FIG. 9. Difference in (a,c) the 50°N to 70°N zonal-mean zonal wind (in  $\text{m s}^{-1}$ ) and (b,d) the polar cap  
 852 average zonal-mean temperature (in K) between (a-b) the reduced NOGWD run and the control run and (c-d)  
 853 the increased NOGWD run and the control run.





854 FIG. 10. Composites of all SSWs for the control run (solid black), reduced NOGWD run (dot-dashed red)  
 855 and increased NOGWD run (dashed blue) with the free-running model. Thick black line shows composites of  
 856 SSWs from the ERA-Interim reanalysis between 1979 and 2016: (a) Zonal-mean zonal wind anomaly at 60°N  
 857 and 10 hPa (in  $\text{m s}^{-1}$ ); Polar-cap average (from 70°N to 90°N) zonal-mean temperature anomalies (in K) at (b)  
 858 1 hPa; (c) 10 hPa; and (d) 50 hPa.